Quasiparticle effects in magnetic-field-resilient three-dimensional transmons

J. Krause,[1] G. Marchegiani,[2] L.M. Janssen,[1] G. Catelani,[2,3] Yoichi Ando,[1,*] and C. Dickel[1,†]

[1] *Physics Institute II, University of Cologne, Zülpicher Str. 77, Köln 50937, Germany*
[2] *Quantum Research Center, Technology Innovation Institute, Abu Dhabi 9639, UAE*
[3] *JARA Institute for Quantum Information (PGI-11), Forschungszentrum Jülich, Jülich 52425, Germany*

(Received 26 March 2024; revised 28 June 2024; accepted 11 September 2024; published 24 October 2024)

Recent research shows that quasiparticle-induced decoherence of superconducting qubits depends on the superconducting-gap asymmetry originating from the different thicknesses of the top and bottom films in Al/AlO$_x$/Al junctions. Magnetic field is a key tuning knob to investigate this dependence as it can change the superconducting gaps *in situ*. We present measurements of the parity-switching time of a field-resilient three-dimensional transmon with in-plane field up to 0.41 T. At low fields, small parity splitting requires qutrit pulse sequences for parity measurements. We measure a nonmonotonic evolution of the parity lifetime with in-plane magnetic field, increasing up to 0.2 T, followed by a decrease at higher fields. We demonstrate that the superconducting-gap asymmetry plays a crucial role in the observed behavior. At zero field, the qubit frequency is nearly resonant with the superconducting-gap difference, favoring the energy exchange with the quasiparticles and so enhancing the parity-switching rate. With a higher magnetic field, the qubit frequency decreases and gets detuned from the gap difference, causing the initial increase of the parity lifetime, while photon-assisted qubit transitions increase, producing the subsequent decrease at higher fields. Besides giving a deeper insight into the parity-switching mechanism in conventional transmon qubits, we establish that Al-AlO$_x$-Al Josephson junctions could be used in architectures for the parity-readout and manipulation of topological qubits based on Majorana zero modes.

DOI: 10.1103/PhysRevApplied.22.044063

I. INTRODUCTION

Superconducting quantum circuits, such as qubits, sensors, and amplifiers have drastically improved over the last two decades [1]. This progress has been achieved through careful management of various sources of losses and noise, ranging from adjusting the circuit's geometry to reduce dielectric losses [2,3] to adding extra filtering to protect the samples from external radiation [4]. Furthermore, the exploration of alternative materials shows promise for creating more performant devices, a recent example being the transmon qubit [5] based on tantalum capacitors [6]. In light of the reduction of other noise sources, nonequilibrium quasiparticles could eventually represent a relevant source of decoherence, in addition to already being a main cause of residual excitations [7].

Moreover, recent reports of chip-wide correlated decoherence due to quasiparticles [8,9] show that quasiparticle loss is a major obstacle to scaling-up superconducting quantum processors. A wide range of solutions to quasiparticle loss is being explored: quasiparticle traps [10], pumping [11], gap engineering [12–15], phonon down-conversion [16,17], optimizing device geometry [18], shielding and filtering [19] or even shielding the device from cosmic rays [20–22]. Magnetic-field-resilient transmons made of thin-film Al/AlO$_x$/Al Josephson junctions (JJs) [23] provide yet another angle to tackle quasiparticle loss: the in-plane magnetic field tunes *in situ* both the transmon transition frequencies and the superconducting gaps of top and bottom aluminum electrodes, making these transmons an ideal system to study quasiparticle effects and optimize gap engineering.

In a parallel effort, magnetic-field-resilient transmons with aluminum tunnel JJs can be a key component for topological quantum-computation protocols based on precise readout and control of the fermion parity of Majorana zero modes (MZMs). Circuit QED measurements [24] of offset-charge-sensitive transmon circuits allow for robust and fast detection of charge-parity switching [7,25], and hence transmons incorporating topological-superconductor nanowires provide an ideal platform to measure and manipulate MZMs [26,27]. To host MZMs, the wires typically need to be threaded by large parallel magnetic fields on the order of at least 0.5 T, posing strong requirements on the magnetic field resilience of the readout circuitry, too. In this context hybrid JJs for field compatible transmons have also been explored [28–31]. With

---

[*] Contact author: ando@ph2.uni-koeln.de
[†] Contact author: dickel@ph2.uni-koeln.de

magnetic-field-resilient aluminum transmons, the advantages of highly coherent and reliable tunnel junctions can be exploited to achieve high-fidelity parity measurements even in large magnetic fields.

In this paper, we present measurements of the quasiparticle-induced parity-switching rates in a three-dimensional (3D) transmon [32] as a function of in-plane magnetic field up to 0.41 T, promoting thin-film aluminum transmons for the parity readout of future topological qubits. Using a comprehensive model, we distinguish the relevant mechanisms of parity switching, providing evidence for an interplay between Cooper-pair-breaking photons, the superconducting gaps in both sides of the JJs, and the Fraunhofer effect in the JJs. We report signatures of near-resonantly enhanced quasiparticle tunneling due to the superconducting-gap difference approaching the transmon frequency at low in-plane magnetic fields; this resonance condition is gradually lifted with increasing fields until photon-assisted parity switching dominates. Thus, counterintuitively, the maximum parity lifetime is reached at a finite field of about 0.2 T. Measurements of the temperature dependence of the parity-switching time for selected in-plane magnetic fields further support these findings. We use different transmon transitions in the parity measurements [33,34], as the Josephson energy changes with the magnetic field, mainly due to the Fraunhofer effect. Our results complement recent experimental [35,36] and theoretical [37] works on the impact of gap asymmetry on the quasiparticle decoherence rate of transmons.

This paper is organized as follows. In Sec. II we discuss the experiment design, while in Sec. III the magnetic-field-dependent spectrum is shown and parameters of the transmon are determined by modeling it. Section IV is devoted to the in-plane magnetic field dependence of the parity-switching time and Sec. V to its temperature dependence for selected in-plane magnetic fields. In the Conclusions [Sec. VI], we summarize the results and give an outlook for future research.

II. EXPERIMENT DESIGN

The experiment is conceived to measure the effect of magnetic fields on the parity-switching time τ_p of an offset-charge-sensitive transmon [38]. For dispersive readout, the transmon is coupled to a 3D copper cavity [Fig. 1(a)], which is unaffected even by large magnetic fields. We use a bias tee at one of the cavity pins to apply an offset voltage V_g to the two transmon islands (see Appendix A for details of the setup and Appendix B for the device fabrication and geometry). In this way, we can measure the charge dispersion, the dependence of the spectrum on the offset charge $n_g \propto V_g$.

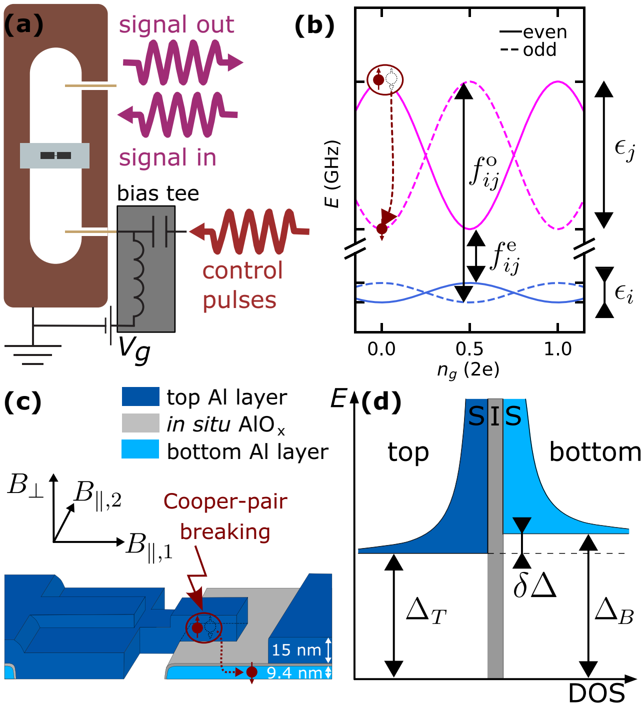

FIG. 1. Schematic of the experiment design. (a) Sketch of the 3D copper cavity with the transmon. A bias tee at one of the cavity pins enables voltage biasing (V_g) of the transmon. (b) Successive transmon energy levels i and j as a function of the offset charge n_g (proportional to V_g). There are two manifolds ("even" and "odd") connected by the incoherent tunneling of single quasiparticles. Energy levels have a charge dispersion with peak-to-peak value ϵ_i and transition frequencies f^{e}_{ij} and f^{o}_{ij}. (c) Sketch of a Dolan-bridge Josephson junction (JJ) relating the magnetic field axes to the JJ geometry. A vector magnet is used to flux bias the SQUID loop along $B_\perp$ and to apply in-plane magnetic fields along $B_{\parallel,1}$ and $B_{\parallel,2}$. Quasiparticles can be generated by Cooper-pair-breaking photons; any event where single quasiparticles tunnel through the JJ changes the charge parity of both electrodes and makes the transmon transition frequencies jump from f^{e}_{ij} to f^{o}_{ij} or vice versa. The two electrodes in the JJ have different thicknesses for the top and bottom aluminum layers, leading to different superconducting gaps in the excitation spectrum. (d) Density of states (DOS) and superconducting gap for the two electrodes.

The charge dispersion is $2e$ periodic, where e is the elementary charge (for transmon Hamiltonian see Appendix C). We define the peak-to-peak variation of transmon level i as ϵ_i. However, the transmon energy spectrum splits into two separate manifolds that differ by one electron charge [see Fig. 1(b)] and are labeled "even" and "odd." Microwave transitions are only possible within each manifold with frequencies f^{e}_{ij} and f^{o}_{ij}, respectively, but not between them, as this would require a term in the Hamiltonian that connects them [39]. The two manifolds are incoherently connected by the tunneling of single quasiparticle excitations across the junction [40–42]. This is equivalent to a 1/2 shift in n_g (a shift by $1e$), which changes the transmon transition frequencies from f^{e}_{ij} to f^{o}_{ij}

or vice versa and can be accompanied by qubit relaxation or excitation. We define the transmon parity as the parity of the number of single quasiparticles that have tunneled across the junction [35] and the parity-switching time τ_p as the mean dwell time between two such events. In addition to the discrete parity jumps caused by quasiparticles tunneling across the junction, the charge environment creates noise in n_g including slow drift, shifting by about $1e$ over a time scale of order 10 min. The transmon was introduced [43] as a qubit design less sensitive to noise in n_g, but charge noise in transmons continues to be a subject of research [44].

Our transmon includes a superconducting quantum interference device (SQUID) comprising two Al/AlO$_x$/Al tunnel junctions. Thin aluminum films yield relatively high critical fields $B_\mathrm{c} \sim 1$ T for magnetic fields applied in plane [45,46], and narrow superconducting electrodes minimize vortex losses. Previously, we showed that a device based on the same geometry can remain sufficiently coherent (with lifetimes of the order of 1 μs) even at high magnetic fields [23]. The two superconducting electrodes composing each junction are characterized by different superconducting gaps, Δ_B and Δ_T, due to the different film thicknesses of the bottom (B) and top (T) aluminum layer [Figs. 1(c) and 1(d)]. The gap asymmetry $\delta\Delta = \Delta_B - \Delta_T$ estimated with a phenomenological law [37,47,48] is on the order of the transmon transition energy hf_{01}, making it relevant for quasiparticle-tunneling processes [37]. A SQUID transmon was chosen such that at low fields, the bottom sweet spot has a sufficient charge dispersion for charge-parity measurements, while at higher fields eventually, the top sweet-spot charge dispersion becomes sufficient. However, due to flux instabilities, we could not measure the spectrum for $B_{\parallel,1} > 0.41$ T for reasons that are currently not understood. Coherence times start to drop sharply slightly below 0.40 T (see Supplemental Material [49] for details). Due to flux noise, the qubit coherence is severely reduced away from the top and bottom sweet spots of the SQUID, so measurements of the parity-switching time were mainly performed at the bottom sweet spot.

A vector magnet is used to flux-bias the SQUID loop with an out-of-plane field $B_\perp$ and to apply in-plane magnetic fields along $B_{\parallel,1}$ and $B_{\parallel,2}$ [see Fig. 1(c)]. The frequency modulation due to the SQUID is highly sensitive to $B_\perp$, which enables precise alignment of the magnetic field to the sample plane to within $\pm 0.05^\circ$. To measure the magnetic field dependence of the parity-switching time, we apply the field along the $B_{\parallel,1}$ axis. Previously we saw that the magnetic field dependence along the $B_{\parallel,2}$ axis was more erratic [23], which we hypothesize to be due to different spurious JJs in the two field directions. In the following, we will use $B_\parallel$ as a shorthand for $B_{\parallel,1}$.

III. IN-PLANE MAGNETIC FIELD DEPENDENCE OF THE TRANSMON SPECTRUM

First, we investigate the evolution of the transmon spectrum with the applied magnetic field to extract the parameters of our device, such as the Josephson energy (E_J) and the charging energy (E_C). The in-plane magnetic field $B_\parallel$ modulates E_J, while E_C remains unaffected. Consequently, the transmon spectrum changes as a function of $B_\parallel$; both the transition frequencies between different transmon levels and their respective charge dispersions are modified.

Two different mechanisms contribute to the suppression of the Josephson energy E_J in the presence of an in-plane magnetic field. First, the magnetic field weakens superconductivity in the two electrodes composing the SQUID [50]. Specifically, the superconducting gaps Δ_B, Δ_T, and so $E_\mathrm{J} \propto \Delta_B\Delta_T/(\Delta_B + \Delta_T)$, decrease monotonically with increasing $B_\parallel$. Second, the magnetic field directly affects the Josephson coupling at the junction by laterally penetrating the JJ's oxide barrier. This causes a Fraunhofer-like pattern in the dependence of the junction's critical current I_c on $B_\parallel$ [50] (cf. Fig. 8); this modulation is significant when the lateral flux associated with the field is of the order of the superconducting flux quantum $\Phi_0 = h/(2e)$ (with h Planck's constant). In our case, with JJs of width $l_2 \sim 200$ nm and film thickness $t \sim 10$ nm [51], this field is of order $B_{\Phi_0}(t, l_2) \sim \Phi_0/(l_2 t) \sim 1$ T. We were able to explore this regime here due to the large in-plane critical field B_c of thin-film superconducting electrodes [46]. In typical JJs, the electrodes are thicker, usually 30 nm and above; as the critical field B_c decreases faster with thickness than B_{Φ_0} ($t^{-3/2}$ [46] vs t^{-1}), the Fraunhofer effect becomes less relevant as thickness increases.

To quantify both contributions to E_J, we measure the perpendicular flux dependence of the lowest energy transitions in a SQUID transmon for selected in-plane magnetic fields $B_\parallel$ [Fig. 2(a)]. The SQUID is asymmetric; the two JJs have different dimensions, and hence different Josephson energies $E_{\mathrm{J}a}$ and $E_{\mathrm{J}b}$ proportional to the junction area. Therefore, the flux arcs shown in Fig. 2(a) display both a top and a bottom flux sweet spot, for which $E_\mathrm{J}(\Phi = 0) = E_{\mathrm{J}a} + E_{\mathrm{J}b}$ and $E_\mathrm{J}(\Phi = 0.5\Phi_0) = |E_{\mathrm{J}a} - E_{\mathrm{J}b}|$, respectively. The inset of Fig. 2(a) shows the extracted Josephson energies as a function of $B_\parallel$. In general, the magnitude of gap suppression at a given field is determined by material properties and film thickness; since the two arms of the SQUID have been fabricated simultaneously, we take the two junctions to be equally affected by gap suppression. In contrast, the characteristic fields for the Fraunhofer contribution to I_c are different ($B_{\Phi_{0,a}} \neq B_{\Phi_{0,b}}$) due to the SQUID asymmetry. Consequently, the parameter characterizing the SQUID asymmetry $\alpha_\mathrm{JJ} = |E_{\mathrm{J}a} - E_{\mathrm{J}b}|/(E_{\mathrm{J}a} + E_{\mathrm{J}b})$ changes with $B_\parallel$; this feature allows us to discriminate

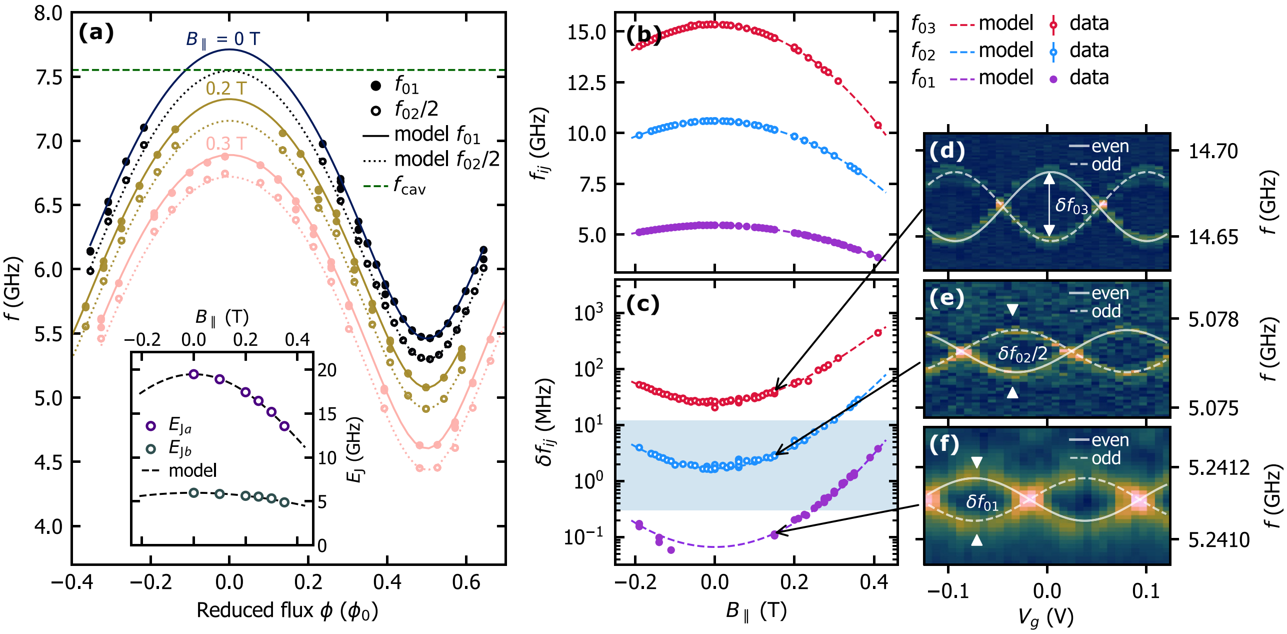

FIG. 2. Transmon spectroscopy in a magnetic field. (a) Transmon frequencies $f_{01}, f_{02}/2$ as a function of $B_\perp$ (here expressed as the reduced flux Φ/Φ_0) for selected $B_\parallel$. The asymmetric SQUID oscillates between top and bottom flux sweet spots, corresponding to the sum and difference of the two junctions' Josephson energies E_{Ja} and E_{Jb}. For $B_\parallel \leq 0.2$ T the top sweet spot is close to $f_{\rm cav}$ (dashed horizontal line) and therefore we do not perform dispersive two-tone spectroscopy for frequencies above 7.1 GHz. The inset shows E_{Ja} and E_{Jb} as a function of $B_\parallel$. Their monotonic decrease with $B_\parallel$ is mainly due to a Fraunhofer-like pattern in the junctions' critical currents $I_{c,a}$ and $I_{c,b}$; the magnetic field further decreases E_J by suppressing the superconducting gap. However, in the magnetic field range covered by quasiparticle-parity measurements, the effect is small, less than 3% (see Appendix D). (b),(c) In-plane magnetic field dependence of the bottom sweet-spot transitions f_{01}, f_{02}, and f_{03} and their respective parity-frequency splittings $\delta f_{ij} = \max_{n_g}(f_{ij}^{\rm e} - f_{ij}^{\rm o})$. As E_J decreases all f_{ij} decrease, while their δf_{ij} increase; we assume E_C to be unaffected by $B_\parallel$. We obtain the f_{ij} and δf_{ij} in voltage-gate scans as shown in panels (d)–(f). For each transition, two separate frequency branches differ by one missing or extra quasiparticle in each of the transmon's electrodes, making it possible to turn the transmon into a quasiparticle parity meter. The blue-shaded area in panel (d) indicates where δf_{ij} is in a useful range for parity-state mapping. For $B_\parallel \leq 0.3$ T we employ the f_{12} transition, for $B_\parallel \geq 0.25$ T we can also use the f_{01} transition. The joint fit to all f_{ij} and δf_{ij} shown in this figure requires higher harmonics $E_{J,m}\cos(m\phi)$ (with m integer) in the Josephson energy term of the transmon Hamiltonian, for details see Appendix C. We find $E_C/h = 327.5$ MHz and the zero-field Josephson energies $E_{Ja}^0/h = 19.47$ GHz and $E_{Jb}^0/h = 5.97$ GHz.

between the Fraunhofer contribution and the suppression of the superconducting gaps (for details see Appendix D). In the magnetic field range covered by quasiparticle-parity measurements, we estimate the contribution of the gap suppression to $E_J \propto \Delta_B\Delta_T/(\Delta_T + \Delta_B)$ to be less than 3%, so the decrease in E_J is mainly due to the Fraunhofer contribution.

Measuring the parity-switching time requires the transmon to be in an offset-charge sensitive regime. The charge dispersion's peak-to-peak values $\epsilon_i \propto E_C(E_J/E_C)^{i/2+3/4} \exp(-\sqrt{8E_J/E_C})$ [5] depend exponentially on the ratio of E_J/E_C and are larger for higher levels. Experimentally we measure the transition frequencies f_{ij} between two levels $|i\rangle$ and $|j\rangle$ and their parity-frequency splittings $\delta f_{ij} = \max_{n_g}(f_{ij}^{\rm e} - f_{ij}^{\rm o})$. Now, as E_J decreases with $B_\parallel$, the f_{ij} decrease and the δf_{ij} increase. Figures 2(b) and 2(c) show f_{01}, f_{02}, and f_{03} as well as the corresponding δf_{ij} measured at the bottom flux sweet spot as a function of $B_\parallel$. The data is determined from voltage-gate scans like the ones displayed in Figs. 2(d)–2(f); these examples were taken at $B_\parallel = 0.15$ T (see also Appendix E). We observe both frequency branches $f_{ij}^{\rm e}$ and $f_{ij}^{\rm o}$ in two-tone spectroscopy as the measurement is slow compared to the characteristic parity-switching time $\tau_{\rm p}$. In successive single-shot measurements, however, the transmon is either in the "odd" parity state or in the "even" parity state, and parity switches come with a measurable frequency jump. This jump is maximally resolved when the gate voltage V_g is set to the charge sweet spot, i.e., $n_g = 0, 1/2, 1\ldots$ in Fig. 1(b), and it enables a charge-parity meter based on a frequency-dependent gate [25]. To measure the parity-switching rates we use different transmon transitions depending on the field range: for $B_\parallel \geq 0.25$ T, $\delta f_{01} \geq 0.2$ MHz, and we can use the f_{01} transition. For smaller fields, however, the E_J/E_C ratio is on the order of 45 to 30 even for the bottom sweet spot; thus, the charge dispersion is too small for charge-parity measurements, since the waiting time of the Ramsey protocol $\propto 1/\delta f_{01}$ (see also the following section) is longer than our dephasing times. With δf_{02} being a factor 10 larger with comparable dephasing times, we employ the f_{12} transitions instead. That way, we can measure the transmon parity also for higher E_J/E_C ratios and cover a wide range of magnetic fields.

Notably, a joint fit to all f_{ij} and δf_{ij} shown in Fig. 2 requires the inclusion of higher Josephson harmonics $E_{J,m}\cos(m\phi)$ in the transmon Hamiltonian. The data we collected in the process of pursuing the quasiparticle physics shows good evidence for the Josephson harmonics; it has been combined with results from other groups to make the case for a more complex current-phase relationship in conventional Al/AlO$_x$/Al tunnel JJs that had previously been overlooked, see Ref. [52]. Here we explicitly consider the SQUID nature of the transmon in analyzing our data, see Appendix C for details. The parameters we extract from the spectroscopic data, in particular, the charging and Josephson energies, also enter into the estimates of the parity-switching time that we consider in the next section.

IV. IN-PLANE MAGNETIC FIELD DEPENDENCE OF THE PARITY-SWITCHING TIME

We now turn to the characterization of the transmon's parity-switching time as a function of $B_\parallel$. Measurements are performed at the bottom sweet spot in $B_\perp$, see discussion in Sec. II. We use a Ramsey-based parity measurement [25] with superpositions of $|0\rangle$ and $|1\rangle$ as well as $|1\rangle$ and $|2\rangle$, as illustrated in Fig. 3. At a gate-voltage sweet spot ($n_g = 0, 1/2, 1\ldots$), the parity-measurement protocol projects the lower-frequency branch predominantly onto the transmon ground state $|0\rangle$, and the upper-frequency branch onto the first excited state $|1\rangle$. We henceforth call "even" the parity branch that is projected onto $|0\rangle$ and denote its mean dwell time by τ_p^e. Similarly, "odd" is the parity branch that is projected onto $|1\rangle$, with a mean dwell time τ_p^o. As we do not actively reset the transmon state after an individual single-shot parity measurement, we include a waiting time of $5T_1$ before taking the next single-shot parity measurement. As a result, the transmon's first-excited-state population p_1 is on average higher for "odd" than for "even" parity mapping, as the transmon relaxes from the excited state to the ground state during the waiting time, see Fig. 3(c). At the base temperature of the cryostat, $T \sim 7\,\mathrm{mK}$, we estimate a mean excited-state population $\overline{p}_1^e = 4.3\%$ for "even" parity and $\overline{p}_1^o = 19.5\%$ for "odd" parity. More details on the parity-measurement sequence and its analysis in terms of a hidden Markov model can be found in Appendix F.

Figure 4(a) shows the two parity-switching times for "even" (τ_p^e) and "odd" (τ_p^o) parity as a function of $B_\parallel$. Most notably, the two parity-switching times evolve nonmonotonically with $B_\parallel$: for both τ_p^e and τ_p^o we observe an initial increase with applied magnetic field, reaching a maximum at $B_\parallel \approx 0.2\,\mathrm{T}$, before decreasing at higher fields. Besides, we generally observe $\tau_p^e \neq \tau_p^o$; in particular, for $|B_\parallel| \leq 0.2\,\mathrm{T}$, τ_p^o is smaller than τ_p^e. Theoretically, we expect $\tau_p^e \approx \tau_p^o$, since the asymmetry between "even" and "odd" parity-switching rates is at most of order $e^{-h\delta f_{01}/k_B T}$ [53] (with k_B Boltzmann's constant). Even at the nominal base temperature of the cryostat $T_0 \approx 7\,\mathrm{mK}$, we have $k_B T_0/h \approx 150\,\mathrm{MHz} \gg \delta f_{01} \sim 0.1 - 10\,\mathrm{MHz}$ [cf. Fig. 2(c)]. As we will argue below, the difference between τ_p^e and τ_p^o is instead due to the measurement-induced $\overline{p}_1$.

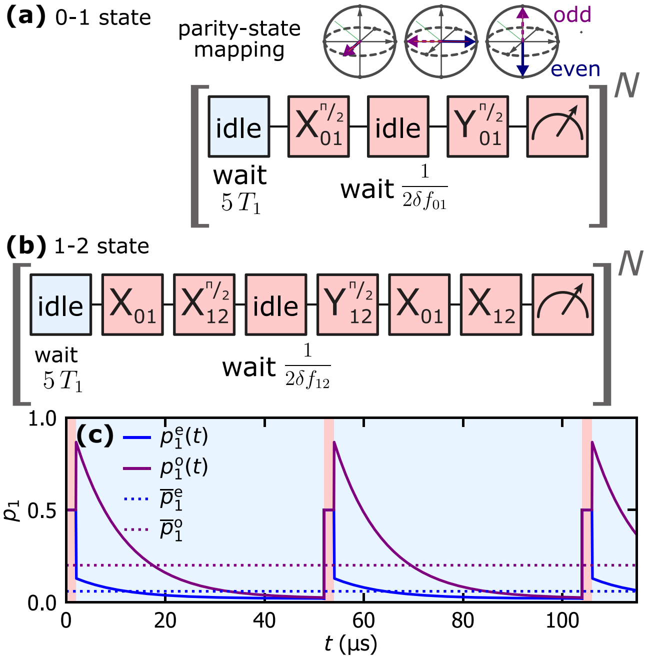

FIG. 3. Parity-mapping scheme. (a),(b) show the gate sequences for the parity measurements using superpositions $|0\rangle + |1\rangle$, and $|1\rangle + |2\rangle$, respectively. They are repeated $N = 2^{18}$ times. For an initial $|0\rangle$ state, we define "even" ("odd") parity as the parity that is ideally mapped on $|0\rangle$ ($|1\rangle$). During the parity-measurement sequence, the transmon is out of equilibrium. (c) estimated excited-state population p_1 for "even" and "odd" parity as a function of time during the parity-measurement cycle. From the hidden-Markov model, we obtain measurement outcomes for declared "even" and "odd" parities, which give the initial populations after the measurement. Finite parity-measurement fidelity leads to slight deviations from the ideal $p_1 = 0$ for "even" parity. Taking the average over the cycle, we can estimate the mean populations $\overline{p}_1^e$, $\overline{p}_1^o$ for the "even" and "odd" parities, which are input parameters for modeling the switching-time data.

A. Modeling the parity-switching time

To understand the nonmonotonic magnetic field dependence of τ_p and the difference between "even" and "odd" parities we model different contributions to the parity-switching time. Adopting the notation of Ref. [35], we distinguish photon-assisted parity switching (PAPS) [54],

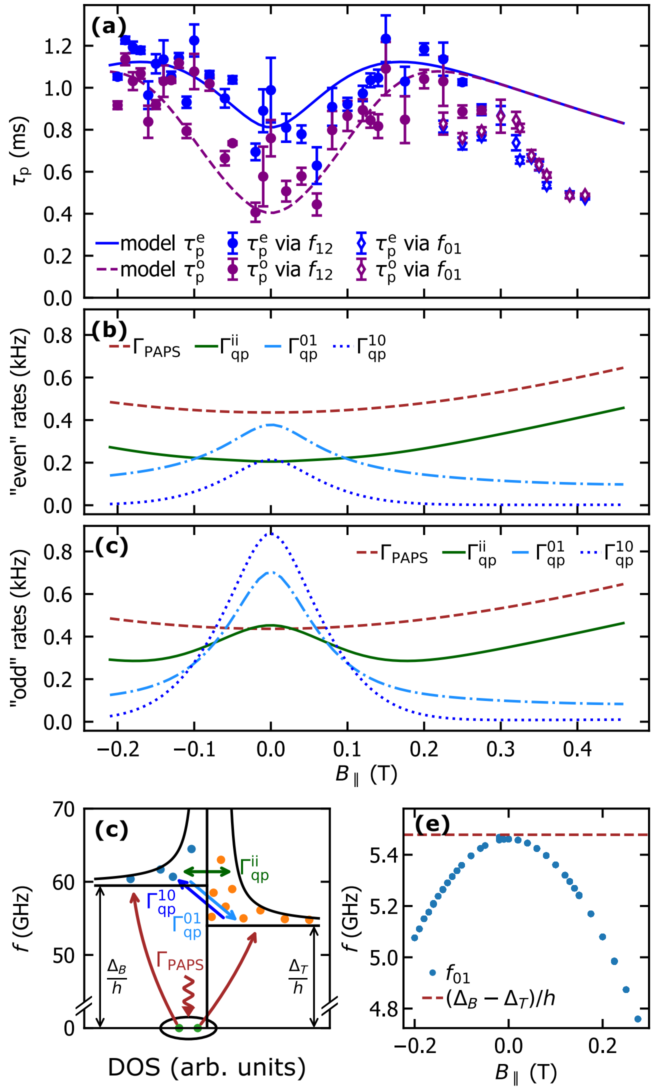

FIG. 4. (a) Parity-switching times τ_p^e and τ_p^o for "even" and "odd" parity vs $B_\parallel$ measured at the flux bottom sweet spot. Model contributions to (b) $1/\tau_p^e$ and (c) $1/\tau_p^o$. Around $B_\parallel = 0\,\mathrm{T}$ the population-weighted quasiparticle-tunneling rates Γ_{qp}^{01} and Γ_{qp}^{10} [Eqs. (5) and (6)] show a peak. These two processes excite or relax the transmon while bridging the superconducting-gap difference and are resonantly enhanced when $f_{01} \simeq \delta\Delta/h$, explaining the low-field dip in τ_p. A higher first-excited-state population p_1 further increases Γ_{qp}^{10} for the "odd" case, which is why $\tau_p^o < \tau_p^e$ in this region. Rate Γ_{qp}^{ii} accounts for quasiparticle tunneling not accompanied by qubit logical state change. Photon-assisted quasiparticle tunneling Γ_{PAPS} dominates for higher fields. (d) Schematic density of states for the quasiparticle excitation spectra in high- and low-gap (bottom and top) electrodes. The quasiparticles are generated by pair-breaking photons; they can tunnel at constant quasiparticle and transmon energy or by exchanging energy with the transmon. (e) Qubit frequency f_{01} and estimated superconducting-gap difference $\delta\Delta/h = (\Delta_B - \Delta_T)/h$ vs $B_\parallel$. While at zero field $f_{01} \simeq \delta\Delta/h$, the transmon is tuned further away from resonance for higher fields. Gaps used for the theoretical curves are $\Delta_T/h = 54\,\mathrm{GHz}$ and $\delta\Delta/h = 5.48\,\mathrm{GHz}$. For the remaining model parameters see Appendix G.

from number-conserving parity-switching (NUPS) events, expressing

$$\frac{1}{\tau_p} = \Gamma_{PAPS} + \Gamma_{NUPS}. \tag{1}$$

For PAPS events, pair-breaking photons with energy larger than the gap sum $\Delta_B + \Delta_T$ are absorbed right at the JJ, leading to the generation of quasiparticles in the bottom and top electrode at a total rate

$$\Gamma_{PAPS} = p_0\left(\Gamma_{00}^{ph} + \Gamma_{01}^{ph}\right) + p_1\left(\Gamma_{11}^{ph} + \Gamma_{10}^{ph}\right). \tag{2}$$

In Eq. (2), p_1 is the occupation probability of the first excited state of the transmon, $p_0 = 1 - p_1$ [we disregard the occupation of higher excitation levels, see discussion in Appendix G], and the subscripts in Γ_{ij}^{ph} denote the initial and final transmon logical states i and j.

In NUPS events, quasiparticles tunnel from one side of the JJ to the other, conserving the total quasiparticle number. We distinguish three terms in the total rate of these events,

$$\Gamma_{NUPS} = \Gamma_{qp}^{ii} + \Gamma_{qp}^{01} + \Gamma_{qp}^{10}. \tag{3}$$

In general, both quasiparticles in the bottom and top electrodes contribute to each term. For instance, for the "quasielastic" events modifying the transmon's parity only but not its logical state (i.e., with exchanged energy $|\epsilon_i| \ll hf_{01}$) their rate takes the form

$$\begin{aligned}\Gamma_{qp}^{ii} &= p_0\left(\tilde{\Gamma}_{00}^{B}x_B + \tilde{\Gamma}_{00}^{T}x_T\right) + p_1\left(\tilde{\Gamma}_{11}^{B}x_B + \tilde{\Gamma}_{11}^{T}x_T\right)\\ &\approx \tilde{\Gamma}_{00}^{B}x_B + \tilde{\Gamma}_{00}^{T}x_T\end{aligned} \tag{4}$$

where x_B, x_T are the dimensionless quasiparticle densities in the bottom and top electrodes, respectively [$x_\alpha = N_\alpha/N_{Cp}^\alpha$, with N_α and N_{Cp}^α the numbers of quasiparticle and the Cooper pairs in electrode α]. The rates $\tilde{\Gamma}_{ij}^\alpha$ denote tunneling of quasiparticles initially located in electrode α into the other electrode with initial and final transmon states i and j. The approximation in the second line of Eq. (4) is valid at leading order in the ratio E_J/E_C for a transmon. For the rates of events changing the transmon state by exchanging energy of about hf_{01} (weighted by the transmon state occupation probability) we consider

$$\Gamma_{qp}^{01} = p_0\tilde{\Gamma}_{01}^{B}x_B, \tag{5}$$

$$\Gamma_{qp}^{10} = p_1\left(\tilde{\Gamma}_{10}^{T}x_T + \tilde{\Gamma}_{10}^{B}x_B\right) \tag{6}$$

for events associated with transmon excitation and relaxation, respectively (see Appendix G about the contribution to $\Gamma_{\mathrm{qp}}^{01}$ from the top electrode's quasiparticles). Note that the excited-state population p_1 is in general determined not just by quasiparticles, but by all the mechanisms affecting the transmon, including measurement as explained above; since p_1 can be determined experimentally, we treat it as an input parameter in analyzing the parity-switching time.

The steady-state values of the quasiparticle densities in the two electrodes x_B and x_T are computed by solving a system of coupled rate equations. Physically, these densities are determined by the balance between processes keeping the quasiparticles away from the junctions, such as recombination and trapping, and quasiparticle generation, which in our model originates from pair breaking by high-frequency photons with rate $\propto \Gamma_{\mathrm{PAPS}}$. Details on the approximate solution to the rate equations and on the temperature and parallel field dependencies of the rates $\tilde{\Gamma}_{ij}^{\alpha}$ and $\Gamma_{ij}^{\mathrm{ph}}$ are given in Appendix G. The parallel magnetic field modulates these rates via three distinct effects: first, E_{J} changes due to a combination of gap suppression and Fraunhofer effect; this also changes the qubit frequency and influences the matrix elements for quasiparticle transitions. Second, similarly to the Fraunhofer modulation of the critical current, these matrix elements are also directly altered by phase-interference effects. Third, the two superconducting gaps get suppressed differently because the critical field depends on film thickness; in modeling the parity-switching time in the following subsection, we can neglect the field dependence of the superconducting gap as we only reach a small fraction of the critical field.

B. Distinguishing parity-switching mechanisms

Figures 4(b) and 4(c) show the magnetic field dependence of the estimated contributions Γ_{PAPS}, $\Gamma_{\mathrm{qp}}^{01}$, $\Gamma_{\mathrm{qp}}^{10}$ and $\Gamma_{\mathrm{qp}}^{\mathrm{ii}}$ to $\tau_{\mathrm{p}}^{\mathrm{e}}$ and $\tau_{\mathrm{p}}^{\mathrm{o}}$, respectively. We first address the nonmonotonic behavior of τ_{p}, so we focus on the "odd" case, where this feature is more prominent. At zero field, the quasiparticle tunneling rates $\Gamma_{\mathrm{qp}}^{01}$ and $\Gamma_{\mathrm{qp}}^{10}$ are maximum, decreasing monotonically with $|B_{\parallel}|$. The transitions described by the rates $\Gamma_{\mathrm{qp}}^{01}$ and $\Gamma_{\mathrm{qp}}^{10}$ excite and relax the transmon, respectively, exchanging an energy approximately hf_{01}. These processes are strongly enhanced when $\Delta_B - \Delta_T \simeq hf_{01}$ due to the large density of states in the quasiparticle spectrum near the gap edge [see Fig. 4(d) and Ref. [37]]. At zero field, the gap difference estimated through fitting slightly exceeds the qubit frequency, i.e., $\delta\Delta \gtrsim f_{01}$. With increasing magnetic field, f_{01} decreases and is progressively detuned from the gap difference [Fig. 4(e)], causing the initial increase of τ_{p} with applied magnetic field. In contrast, photon-assisted pair-breaking increases as E_{J} decreases, producing the subsequent decay of τ_{p} at higher fields. The competition between PAPS and NUPS is similar to the one reported in Ref. [35], where the authors distinguish the two contributions by exploiting the modulation of the frequency of a SQUID transmon with an out-of-plane magnetic field. Here, instead, the interplay of PAPS and NUPS is tuned by $B_{\parallel}$, causing the nonmonotonic evolution of τ_{p}: while PAPS dominates for higher fields, NUPS dominates at low fields. In Ref. [35], the resonant enhancement of quasiparticle tunneling at $\delta\Delta \simeq hf_{01}$ was probed by tuning the frequency via the SQUID modulating $B_{\perp}$. In our setup, the flux noise is more severe likely due to the large vector magnet (it increases with $B_{\parallel,1}$, see Ref. [23]). This makes it impossible to measure τ_{p} away from the bottom sweet spot, where the impact of flux noise is reduced. A flux-dependent measurement, which would serve as a cross-check for the determination of $\delta\Delta$, might be enabled if the susceptibility to external flux noise is reduced by using a gradiometric SQUID transmon [55]. The required local flux-bias line has been demonstrated for 3D transmons [56].

The difference between "even" and "odd" parity-switching times $\tau_{\mathrm{p}}^{\mathrm{e}}$ and $\tau_{\mathrm{p}}^{\mathrm{o}}$ is related to the dependence of the average excited-state population p_1 on the parity measurements: as discussed above, p_1 is higher for "odd" than for "even" parity, because the "odd" parity predominantly ends up in $|1\rangle$ at the end of the parity mapping and then relaxes during the idling, while the even parity predominantly ends up in $|0\rangle$ (see Fig. 3). Quasiparticle transitions with concomitant transmon relaxation at rate $\Gamma_{\mathrm{qp}}^{10}$ require the transmon to be in the excited state and are therefore proportional to p_1. Consequently, the contribution of $\Gamma_{\mathrm{qp}}^{10}$ is enhanced for "odd" parity compared to "even" parity. At the same time, quasiparticle transitions at rate $\Gamma_{\mathrm{qp}}^{10}$ are dominantly from the low-gap (top) electrode to the high-gap (bottom) electrode, since $x_T \gg x_B$ for $\delta\Delta > hf_{01}$ [37]. These transitions further increase the quasiparticle density in the high-gap electrode. As a result, x_B is larger for "odd" parity, thus enhancing the contribution of $\Gamma_{\mathrm{qp}}^{01} \propto x_B$, despite the lower occupation of the ground state $p_0 = 1 - p_1$. Plots of the estimated quasiparticle densities x_B, x_T can be found in the Supplemental Material [49].

At the highest fields, i.e., $0.3\,\mathrm{T} \lesssim B_{\parallel} \lesssim 0.41\,\mathrm{T}$, τ_{p} decays more strongly than the model predicts [see Fig. 4(a)]. This coincides with an overall deterioration of the transmon coherence: the transmon lifetime T_1 and Ramsey-coherence time T_2^* drop by an order of magnitude between $B_{\parallel} = 0.3\,\mathrm{T}$ and 0.41 T (see Sec. IV within the Supplemental Material [49]); relatedly, at $B_{\parallel} \gtrsim 0.3\,\mathrm{T}$ the cavity Q-factor starts to decrease. Above $B_{\parallel} = 0.41\,\mathrm{T}$ we observe an extended magnetic field range where the transmon frequency is very unstable in $B_{\perp}$ and in time and therefore largely not measurable (see Sec. VII within the Supplemental Material [49]). For $0.6\,\mathrm{T} \leq B_{\parallel} \leq 0.8\,\mathrm{T}$ we measure again periodic flux modulation of the cavity frequency, but the SQUID remains unstable around its top sweet spot, hence thwarting our plan to use the top sweet spot for high-field measurements of τ_{p}. In Ref. [23] we also observed an unstable region between $B_{\parallel} = 0.4\,\mathrm{T}$ and

0.5 T with a similar device and suspected spurious JJs in the leads to cause it. Here, these effects may be connected to the reduction of τ_p in a way that we currently do not understand.

The reduction of τ_p with field could also originate from effects that our model does not fully account for. Here we disregard the field dependence of the gaps, since as discussed in Sec. III, we estimate the contribution of the gap suppression to E_J to be less than 3% and therefore account only for the Fraunhofer effect on the quasiparticle-tunneling rates. Moreover, the model uses a simplified description of the pair-breaking photons in terms of a single frequency (monochromatic radiation, see Appendix G). More generally, few or several modes can contribute to the photon-assisted pair-breaking rate, and considering, for example, black-body radiation originating from higher-temperature stages of the refrigerator, the photon-assisted switching rates could increase more strongly than predicted by our model, and even more so if the actual parallel critical fields were smaller than our present estimate.

V. TEMPERATURE DEPENDENCE OF THE PARITY-SWITCHING TIME

To complement the data on the magnetic field dependence of τ_p, we measured its temperature dependence for selected in-plane magnetic fields $B_\parallel$. Figures 5(a) and 5(b) show the temperature dependence of "even" and "odd" parity-switching times $\tau_\mathrm{p}^\mathrm{e}$ and $\tau_\mathrm{p}^\mathrm{o}$ for $B_\parallel = 0\,\mathrm{T}$ and $B_\parallel = -0.13\,\mathrm{T}$ (which is close to the maximum observed τ_p; measurements performed at additional values of $B_\parallel$ can be found in Ref. [49]). Interestingly, we observe a cascading decay of τ_p starting already at relatively low temperatures of order $T \sim 50\,\mathrm{mK}$. This behavior cannot be explained by quasiparticle generation due to thermal phonons alone; indeed, this contribution is exponentially suppressed as $\exp(-2\Delta_T/T)$ and typically dominates over pair-breaking photons only at higher temperatures (see Appendix I and Ref. [57]). A similar temperature dependence has been observed but not explained at finite field in a semiconducting nanowire-based transmon [31]. At zero field and in tunnel-junction-based transmons, a decrease in τ_p with temperature has been attributed to the excitation of quasiparticles out of superconducting traps by phonons [18] and more recently related to the gap asymmetry [36].

Our model can capture the cascading decay by taking into account, along with the gap asymmetry, two distinct effects: the thermal broadening of the quasiparticle energy distributions and an increase in the excited-state population p_1. To illustrate these points, we consider the same contributions determining τ_p in our model as in the previous section, now additionally accounting for the temperature variation [Figs. 5(c) and 5(d)]. The contribution Γ_PAPS from photon-assisted parity switching is temperature independent in the measured range [58]. At base temperature $T \sim 7\,\mathrm{mK} \ll \delta\Delta/k_\mathrm{B}$ quasiparticle tunneling rates that leave the transmon state unchanged are slower, $\Gamma_\mathrm{qp}^\mathrm{ii} < \Gamma_\mathrm{PAPS}$; quasiparticles are mainly located in the lower-gap electrode with energy approximately Δ_T, and rates for events where they tunnel from the bottom to the top electrode without changing the qubit logical state are suppressed as $e^{-\delta\Delta/k_\mathrm{B}T}$. Starting from $T \gtrsim 50\,\mathrm{mK}$, the excited-state population p_1 increases [see Fig. 5 panels (e) and (f)], and so the (weighted) rate Γ_qp^{10} increases. Since this process leads to a larger quasiparticle density in the high-gap (bottom) electrode (see plots within the Supplemental Material [49]), the rates Γ_{01}^qp and $\Gamma_\mathrm{ii}^\mathrm{qp}$ are enhanced, too.

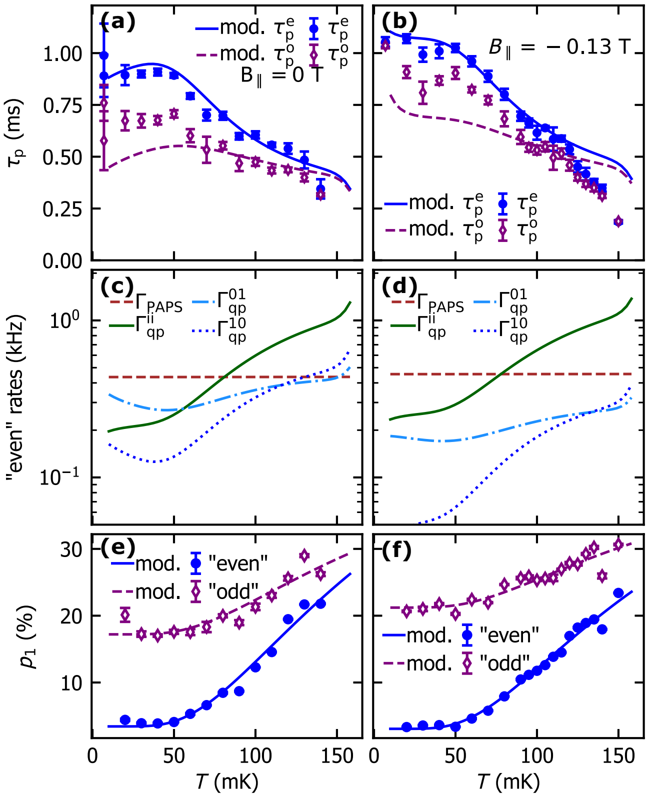

FIG. 5. Temperature dependence of τ_p for (a) $B_\parallel = 0\,\mathrm{mT}$ and (b) $B_\parallel = -0.13\,\mathrm{T}$. A cascading decay starting already around $T \sim 50\,\mathrm{mK}$ cannot be explained by quasiparticle generation due to thermal phonons. (c),(d) Model contributions to $1/\tau_\mathrm{p}^\mathrm{e}$ for both fields. The increase in quasiparticle tunneling with temperature is dominantly caused by enhanced "quasielastic" tunneling $\Gamma_\mathrm{qp}^\mathrm{ii}$ due to a change in the quasiparticle distributions. Two different processes contribute here: first, an increasing excited-state population p_1 enhances Γ_qp^{10}, resulting in an increasing high-gap quasiparticle density. Additionally, a thermal broadening of the quasiparticle energy distributions in bottom and top electrode yields more quasiparticles that can tunnel at a given energy. (e),(f) Temperature dependencies of p_1. The semiphenomenological expression for the fits in these panels is discussed in Appendix H.

The increase of $\Gamma_{\text{ii}}^{\text{qp}}$ is also assisted by the thermal broadening of the quasiparticles distributions [see Fig. 4(d)]. All these processes gradually suppress τ_{p} already for temperatures well below those at which quasiparticles generated by thermal phonons eventually become the limiting factor, $T \gtrsim 150\,\text{mK}$.

The robustness of our modeling is demonstrated by the fact that a fixed set of (few) parameters captures both the magnetic field and the temperature dependencies of τ_{p}. Moreover, the estimated superconducting-gap difference $\delta\Delta = 5.48\,\text{GHz} \cdot h$ is in reasonable agreement with a simple estimate based on a phenomenological law for aluminum thin films [37]. Our estimate for the trapping rates $s_B = s_T = 3.39\,\text{Hz}$ is smaller yet comparable to previously reported values for transmons of similar geometry, which are in the range 10 to 30 Hz [35,59]; we note that when fitting the data, the photon-assisted rate Γ_{PAPS} weakly correlates with $s_B = s_T$. We independently quantify the gap Δ_T, and so the onset of thermal quasiparticles, by fitting the temperature dependence of T_1 measured for different in-plane magnetic fields $B_\parallel$ (Appendix I). The resulting $\Delta_T/h = 54\,\text{GHz}$ slightly overestimates the onset temperature for thermal quasiparticles to dominate the temperature dependence of τ_{p}; accounting for the temperature dependence of the trapping dynamics could perhaps reduce the mismatch. Moreover, the "even" case is generally better described than the "odd" case as the model considers a steady-state solution of coupled rate equations. Our pulse sequence, however, maps "odd" parity to the transmon state $|1\rangle$, repeatedly driving the system away from its steady state. Hence, possible deviations due to the dynamics of the qubit during the measurement of τ_{p} affect more significantly the "odd" assignment.

VI. CONCLUSIONS AND OUTLOOK

We have explored the magnetic field dependence of parity switching times in a 3D SQUID transmon with thin-film Al/AlO$_x$/Al Josephson junctions. The magnetic field provides a tuning knob to explore the physics of quasiparticle dynamics in aluminum tunnel junctions; it suppresses the superconducting gaps Δ_B, Δ_T of both sides of the JJ and it introduces a Fraunhofer-like pattern in the junction's critical current. Both effects can influence the parity switching times. We observe a nonmonotonic evolution of the "even" and "odd" parity-switching times $\tau_{\text{p}}^{\text{e}}$ and $\tau_{\text{p}}^{\text{o}}$ with $B_\parallel$: a dip around $B_\parallel = 0\,\text{T}$ is followed by an initial increase reaching a maximum at $B_\parallel \sim 0.2\,\text{T}$, before decaying at higher fields. The observed maximum parity-switching time (τ_{p}) of 1.2 ms is below the current state of the art on the order of a minute [17,60], but the shielding and filtering of our setup are not as advanced as those used in these works, and the 3D transmon has an antennalike geometry that is more prone to absorption of pair-breaking photons [61,62].

Modeling the quasiparticle dynamics between the two electrodes separated by the JJ with photon-induced pair breaking as a generation mechanism, we explain this behavior by a changing dominant contribution to the parity-switching rate as the magnetic field increases: while photon-assisted parity switching (PAPS) dominates for higher fields, number-conserving parity switching (NUPS) dominates at lower fields. More precisely, NUPS processes Γ_{qp}^{01} and Γ_{qp}^{10} that excite or relax the transmon to bridge the superconducting-gap difference $\delta\Delta$ are resonantly enhanced around zero field as $hf_{01} \simeq \delta\Delta$. The effect is more pronounced for $\tau_{\text{p}}^{\text{o}}$ than for $\tau_{\text{p}}^{\text{e}}$, which we attribute to the additional excited-state population p_1 introduced by our pulse sequence for "odd" parity, which further enhances Γ_{qp}^{10}. While photon-assisted parity switches could likely be reduced by better shielding and filtering, the superconducting-gap difference needs to be carefully engineered to avoid any resonance with transmon transition energies. As this work shows, the magnetic field lifts the resonance condition $hf_{01} \simeq \delta\Delta$ and can, in principle, be used postfabrication as an analog to gap engineering.

To complement the magnetic field data we also measured the temperature dependence of τ_{p} for selected $B_\parallel$. A cascading decay starting already at relatively low temperatures of $T \sim 50\,\text{mK}$ is not due to quasiparticle generation by thermal phonons, as our model helps us understand. Instead, the "quasielastic" tunneling rate $\Gamma_{\text{qp}}^{\text{ii}}$ rapidly increases above this temperature as the quasiparticle energy distributions in the bottom and top electrodes broaden, yielding more available quasiparticles for tunneling at constant energy. Additionally, Γ_{qp}^{10} increases with temperature due to an increasing excited-state population p_1. With the same model parameters, we consistently describe the magnetic field and temperature dependencies of the measured parity-switching times. The model thus helps to identify the relevant tunneling mechanisms and provides insight into how they contribute to the total parity switching rate: Γ_{qp}^{01} and Γ_{qp}^{10} dominantly capture the low-field behavior, Γ_{PAPS} the high field behavior, and $\Gamma_{\text{qp}}^{\text{ii}}$ the temperature dependence.

Our results suggest that Al/AlO$_x$/Al JJ circuits are a viable option for parity readout of topological qubits [27] and that the required magnetic fields do not necessarily cause quasiparticle tunneling to limit the coherence of Al/AlO$_x$/Al JJ circuits. The model we developed can help choose appropriate film thicknesses and junction geometries to approach operation up to 1 T. Moreover, magnetic fields can help in understanding and optimizing gap engineering, as they provide a way to *in situ* change the superconducting gap without heating the sample. In samples with large gap asymmetry, the difference in critical fields will be more pronounced; hence, magnetic fields will strongly change the gap difference elucidating its impact on quasiparticle dynamics.

The setup was controlled based on QCoDeS drivers and logging [63], while the measurements were run using Quantify-core and the time-domain experiments were defined and compiled to hardware using Quantify-scheduler [64,65]. In the data analysis, we used qutip for modeling a qutrit Lindblad equation [66] and hmmlearn for fitting a Gaussian hidden-Markov model to analyze the parity-switching datasets [67].

Datasets and analysis in the form of Jupyter notebooks that create the figures of this manuscript are available on Zenodo [68].

ACKNOWLEDGMENTS

We acknowledge Ioan Pop, Dennis Willsch, and the other authors of Ref. [52], for help in modeling and understanding the spectroscopic data. We also thank Dennis Willsch for his feedback on a draft of the manuscript. We would like to thank Philipp Janke for contributing to data analysis during a student internship. We thank Kelvin Loh, M. Adriaan Rol, and Garrelt Alberts from Orange Quantum Systems for developing software with us to compile the time-domain sequences to the Zürich Instruments hardware. We thank Michel Vielmetter for supporting the time-domain software development. We thank Jurek Frey and Felix Motzoi for discussions on improving the parity-to-state mapping sequences. We thank Lucie Hamdan and Timur Zent for their technical assistance. This project has received funding from the European Research Council (ERC) under the European Union's Horizon 2020 research and innovation program (Grant Agreement No 741121) and was also funded by the Deutsche Forschungsgemeinschaft (DFG, German Research Foundation) under CRC 1238 - 277146847 (Subproject B01) as well as under Germany's Excellence Strategy - Cluster of Excellence Matter and Light for Quantum Computing (ML4Q) EXC 2004/1 - 390534769. G.C. acknowledges support by the German Federal Ministry of Education and Research (BMBF), under the funding program "Quantum technologies—from basic research to market", project "Quantum Computer in the Solid State" (QSolid) (Grant No. 13N16149).

The project was conceived by C.D. and Y.A. Then, J.K. and C.D. fabricated the device and took the measurements with help from L.M.J. The data was analyzed by J.K. and C.D. with help from L.M.J. The theoretical model was extended to the magnetic field by G.M. and G.C. and fit to the data by J.K. and G.M. The paper was written by J.K., G.M., G.C., and C.D. with input from all coauthors.

APPENDIX A: EXPERIMENTAL SETUP

The transmon is mounted in a 3D copper cavity, which is loaded into a bottom-loading dilution refrigerator (Triton 500, Oxford Instruments) with a nominal base temperature of approximately 7 mK. Inside the loading puck, the cavity was wrapped in Eccosorb LS-26 foam to improve the radiation shielding. This might be necessary because the outside of the puck sees the still plate environment, which is at about 1 K.

A detailed wiring diagram of the experiment can be found in Fig. 6. An Eccosorb filter on the input line filters high-frequency radiation. However, the output line remained unfiltered to avoid signal loss. Consequently, potential high-energy photons coming from the LNF-LNC4_8C HEMT amplifier at the 4 K plate may leak back into the cavity to generate quasiparticles. Likely filtering of the output line is currently the easiest way to reduce the Cooper-pair-breaking radiation in the setup.

To voltage bias the device we use a bias tee at one of the cavity pins. The voltage is applied relative to the ground of the dilution refrigerator, which is connected to the copper cavity, while the transmon islands are both floating. The cavity pin couples asymmetrically to the two islands enabling efficient charge bias (see Appendix E).

The temperature control is done via a PID loop using the Lakeshore resistance bridge of the dilution refrigerator. We took care to always stabilize for about 10 min at every temperature to make sure the transmon reaches equilibrium. All temperature readings are based on the mixing chamber $\mathrm{RuO_x}$ thermometer. To check the thermalization, we also looked at the transmon temperature based on ground-state occupancy measurements with the transmon nominally in the ground state (for details see Supplemental Material [49]). At the base temperature the transmon temperature is about 50 mK.

The transmon is controlled with standard DRAG pulses [69,70]. Predominantly the gate times for π and $\pi/2$ pulses were 20 ns. The pulse amplitude is optimized based on Rabi sequences, the frequency based on Ramsey sequences (including beating) and the DRAG parameter is optimized based on an *XY* sequence [71]. While the transmon control pulses and continuous-wave tones were routed to the input port of the cavity, we measured the cavity in reflection via the circulator. The transmon readout was performed without a parametric amplifier. Nonetheless, typical assignment fidelities of >90 % could be achieved for the qubit subspace with readout durations around 1 μs.

APPENDIX B: DEVICE FABRICATION, GEOMETRY, AND FILM THICKNESS

The 3D transmon used in this experiment was fabricated in the same batch and with the same capacitor geometry as the device in Ref. [23]. The aluminum film thickness plays a crucial role in making the transmon magnetic field resilient, but in the thin-film limit, it also has a strong effect on the magnitude of the superconducting gap [37,47,48,72]. In Ref. [23], the nominal film thicknesses for the two aluminum layers according to the Plassys MEB

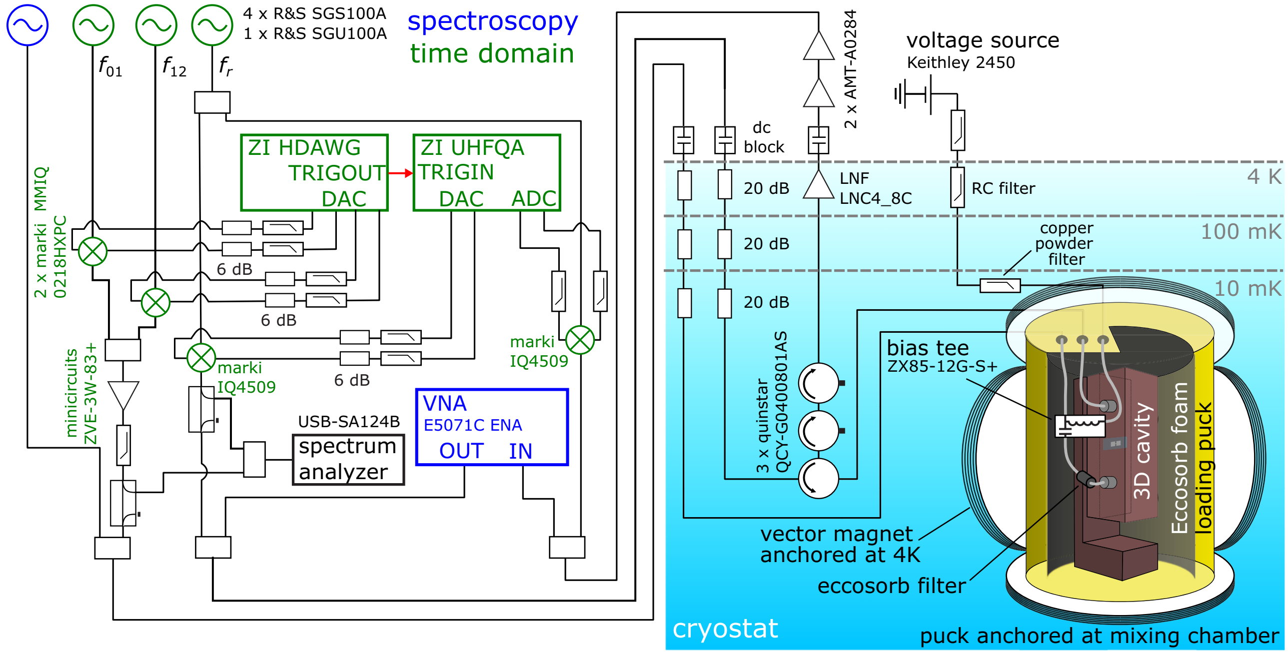

FIG. 6. Wiring diagram of the experiment with the setup for spectroscopy using a two-port Vector Network Analyzer (VNA) and an additional microwave source and the time-domain setup using analog-to-digital converters (ADCs), digital-to-analog converters (DACs), and mixers. The transmon is inside a 3D copper cavity that is in the puck of the bottom loading dilution refrigerator.

550S evaporator used for the film deposition were reported to be 10 nm and 18 nm. The deposition rate was 0.2 nm s^{-1}. Between the two evaporations, the JJ barrier is formed by oxidation in 1 mbar of pure oxygen in a static setting for 6 min. After the second layer, another oxidation step was added to grow the initial oxide in a more controlled way with 1 mbar of oxygen for 10 min.

To measure the film thicknesses and JJ geometry, we perform atomic force microscope imaging of the SQUID region of the device (Fig. 7). The height profile [see Figs. 7(c)–7(e)] shows three characteristic thicknesses at $t_1 = 15.5$ nm for the bottom layer, $t_2 = 21.4$ nm for the top layer, and $t_3 = 31.8$ nm for the double layer. Since these measurements include either one or two additional oxide layers, we estimate the thicknesses t_B and t_T of the bottom and top superconducting electrodes using the following equations:

$$t_1 = t_B + t^{\mathrm{ext}}_{\mathrm{AlOx}}, \tag{B1}$$

$$t_2 = t_T + t^{\mathrm{ext}}_{\mathrm{AlOx}}, \tag{B2}$$

$$t_3 = t_B + t_T + t^{\mathrm{ext}}_{\mathrm{AlOx}} + t^{\mathrm{int}}_{\mathrm{AlOx}}, \tag{B3}$$

where $t^{\mathrm{int}}_{\mathrm{AlOx}}$ and $t^{\mathrm{ext}}_{\mathrm{AlOx}}$ are the thicknesses of the interelectrode and external AlOx insulating barriers, respectively. We assume that, due to the exposure to ambient air and temperature, the oxide layers adding to t_1 and t_2 are the same, regardless of the extra-oxidation step that the bottom layer has faced during fabrication. Assuming that the thickness of the interlayer barrier is approximately $t^{\mathrm{int}}_{\mathrm{AlOx}} \approx 1$ nm, we obtain $t_B \approx 9.4$ nm, $t_T \approx 15.3$ nm and an outer insulating oxide layer of $t^{\mathrm{ext}}_{\mathrm{AlOx}} \approx 6.1$ nm. Notably, the gaps estimated with the phenomenological model $\Delta_{B,T} \approx \Delta^{\mathrm{bulk}}_{\mathrm{Al}} + a/t_{B,T}$ (with $a = 600\ \mu\mathrm{eV/nm}$ and $\Delta^{\mathrm{bulk}}_{\mathrm{Al}} \approx 180\ \mu\mathrm{eV}$, see Ref. [37] and references therein) are $\Delta_B = 59\ \mathrm{GHz} \cdot h$ and $\Delta_T = 53\ \mathrm{GHz} \cdot h$; these values differ by less than 2 % (and their difference by less than 10 %) from the gaps estimated in fitting the measured parity-switching and T_1 times. Figure 7 also clearly shows that the aluminum film is polycrystalline with typical grain sizes on the order of 50 nm and film thickness variations on the order of up to 2 nm.

Additional information on the device stability, coherence times, and transmon temperature is provided in the Supplemental Material [49].

APPENDIX C: JOSEPHSON HARMONICS

The measurements of the frequencies f_{ij} and their parity splittings δf_{ij} of the three lowest logical transmon states unexpectedly cannot be described by the standard Cooper-pair box Hamiltonian

$$H = 4E_C \sum_n (n - n_g)^2 |n\rangle\langle n| - \frac{1}{2}E_J \sum_n (|n\rangle\langle n+1| + |n+1\rangle\langle n|), \tag{C1}$$

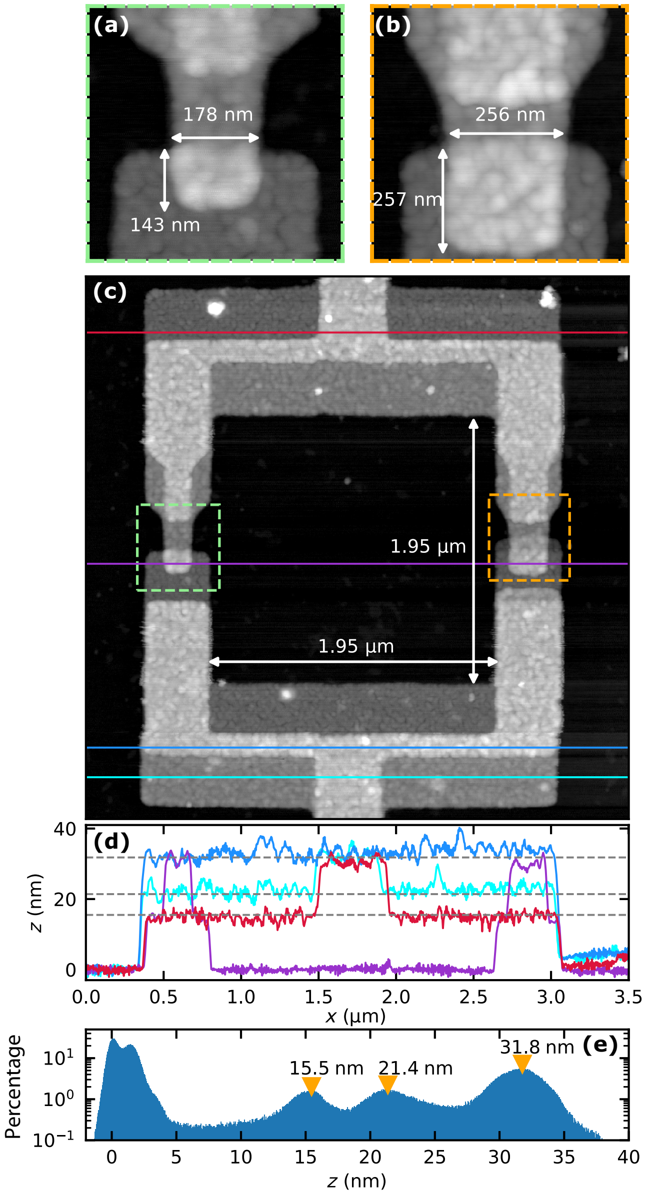

FIG. 7. Atomic force microscope image showing in (c) the SQUID region of the transmon with the dimensions of the SQUID loop. The height is color coded. Panels (a), (b) are magnified images of the JJs and include their lateral dimensions. Aluminum grains with a typical size of 50 nm are visible. (d) Height profiles along the lines indicated in (c). (e) Histogram of the heights in the image with indicated peaks. The three peaks at larger heights correspond to the bottom aluminum layer, the top layer, and the regions where they overlap.

when trying to fit them simultaneously. Here $|n\rangle$ represents the charge-basis state with excess charge $2en$. Related observations by other groups have been combined with our data from this device into a joint publication that reports evidence of deviations from the sinusoidal current-phase relationship for conventional Al/AlO$_x$/Al JJs [52]. A more accurate description of the spectrum requires introducing higher harmonics $E_{\mathrm{J},2}\cos(2\phi)$, $E_{\mathrm{J},3}\cos(3\phi)$,... into the Hamiltonian. In the charge basis, the modified transmon Hamiltonian reads

$$H = 4E_{\mathrm{C}}\sum_n (n-n_g)^2\,|n\rangle\langle n| - \frac{1}{2}\sum_{m=1}^{\infty}\sum_n E_{\mathrm{J},m}\left(|n\rangle\langle n+m| + |n+m\rangle\langle n|\right) \quad \text{(C2)}$$

where the index m identifies the order of the Josephson harmonic. Here we generalize this approach to a SQUID transmon with two junctions a and b; then Eq. (C2) becomes

$$\begin{aligned} H = {} & 4E_{\mathrm{C}}\sum_n (n-n_g)^2\,|n\rangle\langle n| \\ & - \frac{1}{2}\sum_{m=1}^{\infty}\left(E_{\mathrm{J}a,m} + E_{\mathrm{J}b,m}e^{im\phi}\right)\sum_n |n\rangle\langle n+m| \\ & - \frac{1}{2}\sum_{m=1}^{\infty}\left(E_{\mathrm{J}a,m} + E_{\mathrm{J}b,m}e^{-im\phi}\right)\sum_n |n+m\rangle\langle n|, \end{aligned} \quad \text{(C3)}$$

where the phase factors multiplying $E_{\mathrm{Jb,m}}$ account for the (reduced) flux ϕ piercing the SQUID.

To start with, we fit Eq. (C3) to the zero-field data of Fig. 2, including both the perpendicular flux scan for $B_\parallel = 0$ and the f_{ij} and δf_{ij} obtained in voltage-gate scans at bottom sweet spots of the flux arc. We assume that JJs a and b have the same harmonics ratios $E_{\mathrm{J}a,m}/E_{\mathrm{J}a,1} = E_{\mathrm{J}b,m}/E_{\mathrm{J}b,1} \equiv c_m$. The voltage-gate scans of $f_{01}, f_{02}/2, f_{12}$, and f_{03} dominantly determine the Josephson energy at the bottom sweet spot, $E_{\mathrm{J}}(\phi = 0.5) = E_{\mathrm{J}a,1} - E_{\mathrm{J}b,1}$, and the harmonics ratios at the bottom sweet spot,

$$\frac{E_{\mathrm{J}a,m} + (-1)^m E_{\mathrm{J}b,m}}{E_{\mathrm{J}a,1} - E_{\mathrm{J}b,1}} = \begin{cases} c_m & \text{for } m \text{ odd} \\ c_m/\alpha_{\mathrm{JJ}} & \text{for } m \text{ even.} \end{cases} \quad \text{(C4)}$$

The flux scan in turn determines the SQUID asymmetry α_{JJ}. As a result, we find the zero-field Josephson energies $E_{\mathrm{J}a}(0)/h = 19.47$ GHz, $E_{\mathrm{J}b}(0)/h = 5.97$ GHz (corresponding to $\alpha_{\mathrm{JJ}}(0) = 0.53$), and the charging energy $E_{\mathrm{C}}/h = 327.5$ MHz. We find that the higher harmonics decay rapidly with the index m, estimating $c_2 = -0.9\%$ and $c_3 = 0.03\%$. To avoid overfitting, we set the harmonics of order $m \geq 4$ to zero.

We note that our methodology is somewhat different from that employed in Ref. [52]: there, extensive scans of the sets $\{E_{\mathrm{J},m}\}$ of harmonics compatible with the data are performed and the interaction of the transmon with the readout resonator or cavity is taken into account; here we instead just perform a fit to the data using a limited number of harmonics and do not include the effect of the cavity. Thus, we find slightly different results based on the same data. For instance, for the charging energy we obtain a value about 1% lower than the estimate in Ref. [52]. As for the values of the Josephson harmonics, our estimates become smaller with increasing order m compared with those in that reference (by factors of order 1.4 and 13 for c_2 and c_3, respectively, when comparing to the model truncated to four rather than three harmonics).

Hereafter, we drop the label 1 to denote the first Josephson harmonic, i.e., $E_{\mathrm{J}} \equiv E_{\mathrm{J},1}$, and $E_{\mathrm{J}a(b)} \equiv E_{\mathrm{J}a(b),1}$, for notational simplicity.

APPENDIX D: ESTIMATING FRAUNHOFER AND CRITICAL FIELDS

The experimental data analysis of Appendix C yields the zero-field Josephson energies $E_{\mathrm{J}a}(0)$ and $E_{\mathrm{J}b}(0)$ of the SQUID, and their harmonics. The Josephson energies vary as a function of the magnetic field. In this Appendix, we discuss a theoretical model for this dependence to quantify the relative contributions of (i) field suppression of the superconducting gaps Δ_B and Δ_T, (ii) Fraunhofer-like modulation of the Josephson energy, quantified in terms of two characteristic fields $B_{\Phi_{0,a}}$ and $B_{\Phi_{0,b}}$ for JJ$_a$ and JJ$_b$, respectively. We model the field evolution of $E_{\mathrm{J}a}(B_\parallel)$ and $E_{\mathrm{J}b}(B_\parallel)$ by the following expression, also used in Ref. [23]:

$$E_{\mathrm{J}a(b)}(B_\parallel) = E_{\mathrm{J}a(b)}(0)\sqrt{1-\left(\frac{B_\parallel}{B_\mathrm{c}}\right)^2}\left|\mathrm{sinc}\left(\frac{B_\parallel}{B_{\Phi_{0,a(b)}}}\right)\right|, \tag{D1}$$

where $\mathrm{sinc}(x) \equiv \sin(\pi x)/(\pi x)$. The factor in the absolute value in the right-hand side of Eq. (D1) accounts for the Fraunhofer modulation of the Josephson energy for a rectangular junction [73]. Even though thin aluminum films with different thicknesses and gaps display unequal critical fields ($B_\mathrm{c}^B \neq B_\mathrm{c}^T$) [45], we find that a single effective critical field B_c can be used to capture the impact of the gaps' suppression on E_J; the square root in the right-hand side of Eq. (D1) models the gap suppression with a Ginzburg-Landau-type formula $\Delta(B_\parallel)/\Delta(0) = \sqrt{1-(B_\parallel/B_\mathrm{c})^2}$ [50] (see Ref. [74] for the applicability of this approach). The Josephson energy of a JJ with asymmetric gaps is proportional to the harmonic mean of the two gaps, i.e., $E_\mathrm{J} \propto \Delta_B\Delta_T/(\Delta_T+\Delta_B)$, so at the leading order in $B_\parallel \ll B_\mathrm{c}^B, B_\mathrm{c}^T$, Eq. (D1) approximates the expression obtained retaining separately $B_\mathrm{c}^B, B_\mathrm{c}^T$, if we set $B_\mathrm{c}^{-2} = [\Delta_T(0)(B_\mathrm{c}^B)^{-2} + \Delta_B(0)(B_\mathrm{c}^T)^{-2}]/[\Delta_B(0)+\Delta_T(0)]$. The validity of this approach is also supported by the analysis of the cavity frequency shown below.

To start with, we estimate the Fraunhofer fields for the two JJs. While we could not systematically measure the transmon spectrum for $B_\parallel > 0.41$ T, we did measure the cavity resonance frequency f_cav up to 1 T, the limit of our magnet. Sweeping $B_\perp$ by a few hundreds of μT for every $B_\parallel$, we could clearly observe the SQUID oscillations in f_cav mediated by the dispersive shift up to 0.9 T [see Figs. 8(a) and 8(b)]. Around $B_\parallel \simeq 0.8$ T the oscillation collapses, before reviving again for fields $0.82\ \mathrm{T} \leq B_\parallel \leq 0.9$ T. We attribute this behavior to one superconducting flux quantum [$\Phi_0 = h/(2e)$] threading the larger of the two JJs, turning the SQUID effectively into a single-JJ transmon [right arrow in panel (c) of Fig. 8]. Therefore, we estimate $B_{\Phi_{0,a}} = 0.8$ T. Moreover, we observe a local minimum in f_cav around 0.7 T. As indicated by the left arrow in panel (c) of Fig. 8 this minimum corresponds to the condition $E_{\mathrm{J}a} = E_{\mathrm{J}b}$, where the SQUID is symmetric. The resulting near-complete suppression of E_J for half a flux quantum through the SQUID leads to a reduction of the dispersive shift so that f_cav approaches the bare cavity frequency. The intersection of $E_{\mathrm{J}a}$ and $E_{\mathrm{J}b}$ depends only on the zero-field Josephson energies $E_{\mathrm{J}a}(0)$ and $E_{\mathrm{J}b}(0)$, and on the characteristic Fraunhofer fields $B_{\Phi_{0,a}}$ and $B_{\Phi_{0,b}}$, the latter being the only remaining unknown at this point. Requiring $E_{\mathrm{J}a}(0.7\ \mathrm{T}) = E_{\mathrm{J}b}(0.7\ \mathrm{T})$ we estimate $B_{\Phi_{0,b}} = 1.12$ T. As shown in Fig. 8(d) the estimated Fraunhofer fields B_{Φ_0} of JJ$_a$ and JJ$_b$ are inversely proportional to the laterally penetrated junction width l_2, with a proportionality constant that agrees well with that for other devices from the same fabrication batch and that were measured in two-tone spectroscopy up to 1 T [23].

To determine the effective critical field B_c we substitute Eq. (D1) into the Hamiltonian that includes the higher Josephson harmonics, Eq. (C3), and fit the spectroscopic data for the qubit transitions and parity-frequency splittings in Figs. 2(b) and 2(c) [also reproduced in Figs. 9(a) and 9(b)]. For the higher harmonics, as in Appendix C we keep only those with $m = 2$ and 3, and assume their ratios c_m to be independent of parallel field (see end of this Appendix about this assumption). Using this procedure, we estimate $B_\mathrm{c} = 1.85$ T. The actual B_c is likely lower, given that we fit a Ginzburg-Landau dependence and for thin films at low temperatures one expects a faster suppression of Δ close to the critical field [74]. Indeed, we do not observe SQUID oscillations in f_cav for $B_\parallel \geq 0.92$ T, and the critical field estimated for similar devices is about 1 T [23]. We also note that the fitted value of the critical field might in part account for the field-dependent effects, not included in the model, that we discuss at the end of this Appendix; in this context, one can regard B_c as an effective critical field that makes possible a more accurate modeling of the spectroscopic data. Figure 9 shows the fit including the residuals. As in Appendix C, the voltage-gate scans of f_{01}, $f_{02}/2$, f_{12}, and f_{03} dominantly determine the Josephson energy at the bottom sweet spot, $E_\mathrm{J}(B_\parallel, \Phi = 0.5) = E_{\mathrm{J}a}(B_\parallel) - E_{\mathrm{J}b}(B_\parallel)$. Fitting the remaining perpendicular flux scans for fields $B_\parallel > 0$, we can further determine $\alpha_\mathrm{JJ}(B_\parallel)$, and hence the data points for $E_{\mathrm{J}a}$ and $E_{\mathrm{J}b}$ shown in the inset of Fig. 2(a) [also in Fig. 8(c)]. We find their field dependence to be well described by

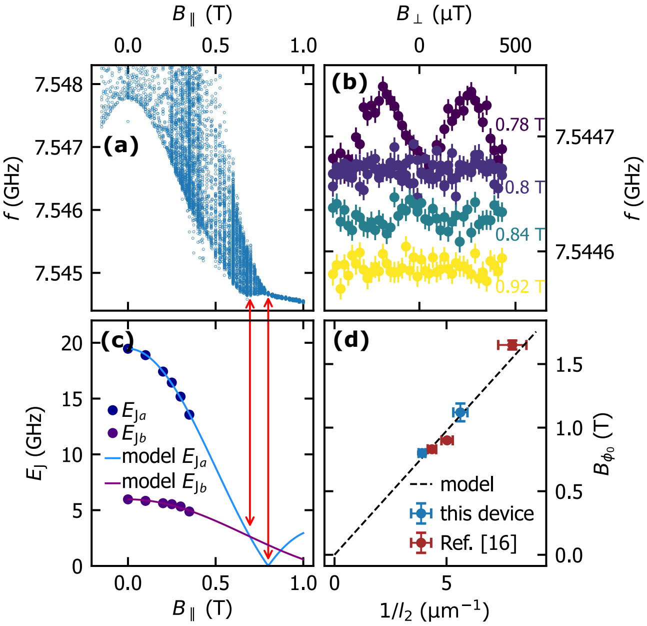

FIG. 8. Estimation of the Fraunhofer modulation of the Josephson energy. (a),(b) Measurements of the resonance frequency f_{cav} of the cavity for different values of the out-of-plane ($B_\perp$) and in-plane ($B_\parallel$) magnetic field plotted against (a) $B_\parallel$ and (b) $B_\perp$ for selected values of $B_\parallel$. The cavity is coupled to the transmon; the periodic oscillations of the transmon frequency with $B_\perp$ (due to the SQUID geometry) translate to oscillations in f_{cav} via the dispersive shift. Due to the Fraunhofer effect, the oscillation vanishes at $B_{\Phi_{0,a}} = 0.8$ T (see the text for the explanation). (c) The estimated Josephson energies E_{Ja} and E_{Jb} of the two JJs intersect at $B_\parallel \simeq 0.7$ T, corresponding to the minimum f_{cav} in (a). That way we can estimate $B_{\Phi_{0,b}} = 1.12$ T. (d) The estimated $B_{\Phi_{0,a}}, B_{\Phi_{0,b}}$ are inversely proportional to the JJ width l_2 that is penetrated by $B_\parallel$ (as expected for a rectangular junction [73]) and agree with more direct measurements performed in Ref. [23] on other devices from the same batch.

Eq. (D1) and the fit parameters obtained in the course of this section, showing the self-consistency of our modeling. We note that, for our purposes, it is sufficient to quantify the gap suppression in the magnetic field range covered by measurements of the parity-switching time, $|B_\parallel| \leq 0.41\,\text{T} \ll B_c$. In this field range, the gaps are suppressed by less than 3% compared to the zero-field values, based on Eq. (D1) and the estimated B_c. For this reason, we disregard the field dependence of the gaps in modeling the parity-switching rates.

In closing this Appendix, we note that the assumption that the ratios $E_{J,m}/E_{J,1}$ are independent of parallel field [implying $E_{J,m} \propto \text{sinc}(B_\parallel/B_{\Phi_0})$] is strictly speaking incorrect, since for rectangular junctions the argument [73] leading to the sinc modulation in Eq. (D1) gives $E_{J,m} \propto \text{sinc}(mB_\parallel/B_{\Phi_0})$. Similarly, a contribution to the second harmonic arising from an inductance in series to the junction would change as $[\text{sinc}(B_\parallel/B_{\Phi_0})]^2$ (at leading order in the ratio between Josephson and inductive energies, see the Supplemental Material to Ref. [52]). We disregard these effects for simplicity since an even more accurate modeling of the spectroscopic data is beyond the scope of the present work. Still, we note that the different dependencies of the junction harmonics and inductive corrections on the parallel field could, in principle, be used to distinguish these two contributions.

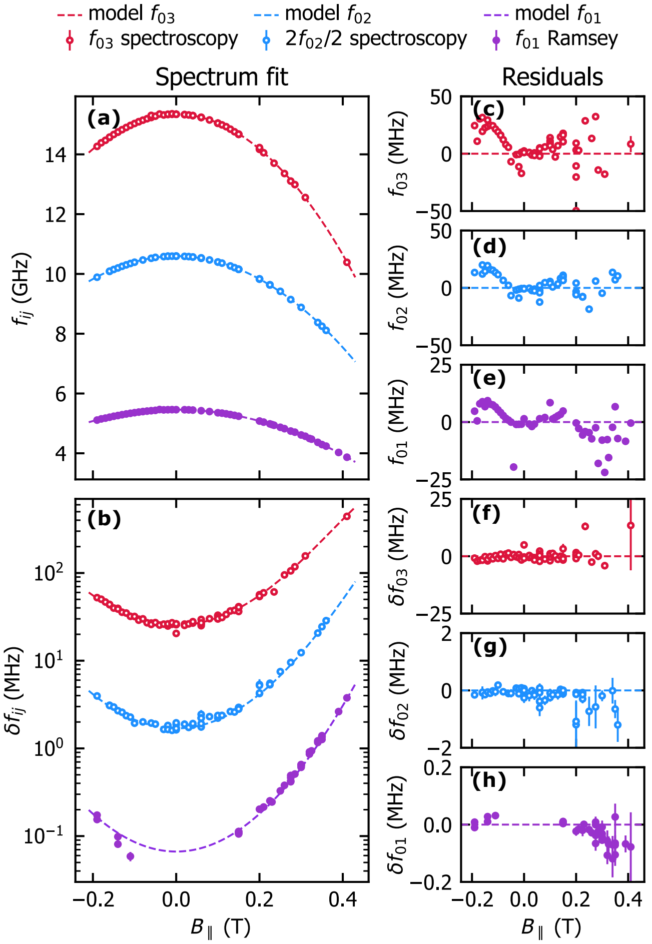

FIG. 9. Transmon transition frequencies f_{ij} (a) and parity-frequency splittings δf_{ij} (b) measured at the bottom sweet spot as a function of $B_\parallel$. The data is obtained from voltage-gate scans like the ones shown in Fig. 2. Substituting Eq. (D1) into Eq. (C3) we estimate $B_c = 1.85$ T based on a fit to the data (see text). Fit residuals (c)–(h) are relatively flat for all f_{ij} and δf_{ij}.

APPENDIX E: GATING THE OFFSET VOLTAGE

In this Appendix, we show that we can control the charge bias of the transmon by applying a dc gate voltage V_g to the bias tee on the cavity input port. Measuring the transmon transitions $f_{01}, f_{02}/2, f_{12}$, and f_{03} as a function of V_g, we observe clear signature of charge-parity splitting for all the transitions (Fig. 2). This feature allows for gate tuning of the transmon to a point of maximum charge-parity

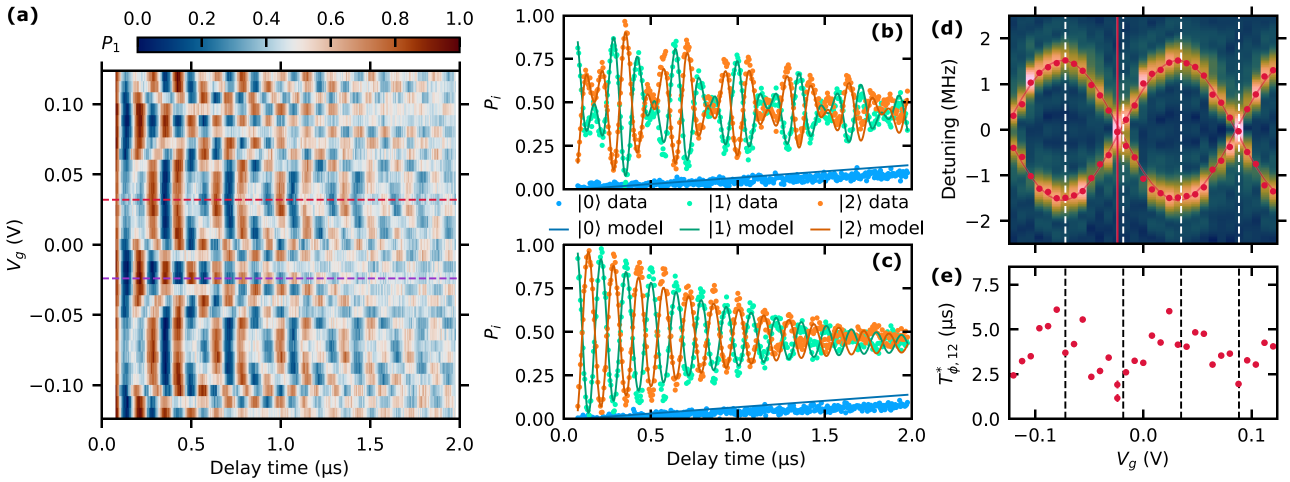

FIG. 10. (a) Ramsey measurement for the 1-2 transition as a function of V_g. The color plot gives the population of $|1\rangle$ as a function of waiting time between the $\pi/2$ pulses and V_g. (b),(c) linecuts of (a) close the charge sweet spot and anti sweet spot. In (b), the characteristic beating for the two parities can be clearly seen. The three-state data is fitted with a qutip [66] simulation. (d) Fourier transform of the temporal data in (a), revealing the charge dispersion directly. Data points are frequencies extracted from the fits to the linescans. (e) Ramsey pure dephasing time $T^*_{\phi,12}$ as a function of gate voltage. While charge noise is not the dominant dephasing process, a slight sweet-spot enhancement can be observed.

splitting, which is the ideal situation to measure the parity-switching time.

Some of the transitions shown in Figs. 2(d)–2(f) were measured in time domain, in a Ramsey-type measurement (see Fig. 10 for an example measurement using a superposition of $|1\rangle$ and $|2\rangle$). Depending on V_g, the Ramsey data shows a beating of two frequency contributions or just a single frequency [see Figs. 10(b) and 10(c)]. A Fourier transform of the Ramsey data [Fig. 10(d)] shows the detuning of the transition energies as plotted in Figs. 2(d)–2(f); here the microwave frequency was chosen at the midpoint between the “even” and “odd” transition frequencies. Accurately fitting the Ramsey data and tuning to this condition is essential for the subsequent parity measurements. The Ramsey pure-dephasing time $T^*_{\phi,12}$ as a function of V_g, Fig. 10(e), is extracted from fitting the linecuts of Fig. 10(a) using relaxation times from a preceding measurement of relaxation from the $|2\rangle$ state (see Supplemental Material [49] for an example). It shows an enhancement at the charge sweet spots but is not T_1 limited as, e.g., flux noise also contributes to $T^*_{\phi,12}$. While Ramsey measurements are sensitive to V_g, measurements of T_1 and T_2^{echo} do not show a V_g dependence [49], suggesting that the dominant charge noise is slow.

We have also explored scanning V_g over many periods and see few jumps and no anomalies [49]. Generally, we find that the V_g scans show the expected double-sinusoidal dependence with few jumps and distortions, but we do find that V_g shows a slight hysteresis when reversing the scan direction. We observe drift in the charge offset at fixed V_g that can cover a period on a timescale of 10 min [44].

APPENDIX F: PARITY-MEASUREMENT SCHEMES

A single parity measurement is realized by a parity-dependent gate on the transmon that flips the qubit state for “odd” parity and leaves it unchanged for “even” parity, followed by a measurement of the transmon state. The parity-dependent gate we use is Ramsey-based [75]; its basic scheme and illustration on the Bloch sphere can be found in Fig. 3(a). The gate requires a careful tuneup: the carrier frequency of the qubit-control pulses needs to be well-centered between “even” and “odd” transmon frequencies f_{e},f_{o} and the voltage gate on the bias tee, V_g, is chosen such that $|f_{\mathrm{e}} - f_{\mathrm{o}}|$ is maximized. Generally, for $\delta f_{ij} < 10$ MHz, our usual 20-ns control pulses are not parity selective, meaning a $\pi/2$ pulse will map both parities onto the same point on the Bloch sphere [see Fig. 3(a)]. The microwave carrier defines a rotating frame, such that the detuning of each parity from the carrier gives the rotation frequency on the Bloch-sphere equator. The detunings have opposite signs, and the parities precess in opposite directions. After a waiting time $t_w = (2\,\delta f_{ij})^{-1}$, the two parities will have rotated to orthogonal states on the Bloch sphere that, with the right rotation, can be mapped to the ground and first-excited states $|0\rangle$ and $|1\rangle$, respectively. The same method can be used with a superposition of $|1\rangle$ and $|2\rangle$ [see Fig. 3(b)]. As explained in Sec. III of the main text, we explore a range of E_J/E_C ratios while sweeping $B_\parallel$, such that the sequences involving higher transitions are useful when the charge dispersion for the 0-1 transition is too small: the charge dispersion increases roughly by a factor of 10 with the level index, while T_1

and T_2^* decrease for the higher levels typically by less than 50%.

In addition to the parity-selective gate, the transmon needs to start in a known state for each run, and a good single-shot readout fidelity for the transmon is required to resolve the parity dynamics. We generally achieve high single-shot fidelities $> 90\%$ that can distinguish $|0\rangle$, $|1\rangle$ and $|2\rangle$ [see Fig. 11(b)]. We let the qubit relax by waiting $5T_1$ between individual runs; at temperatures $\lesssim$50 mK, our qubit has a residual excitation of up to 5 %. In principle, one can also initialize by measurement [25] or just look if the transmon state flips or stays the same compared to the previous measurement.

We then perform the parity-mapping sequence consisting of idling, parity gate, and readout $N = 2^{18}$ times. The measurement results form a sequence of N points in the *IQ* plane, from which the τ_p^e and τ_p^o are determined by fitting a Gaussian hidden-Markov model (HMM) [76]. The hidden parameter in our Markov model is the "true" parity, while the measured parameters are the *IQ* voltages, which have different probability distributions for the $|0\rangle$, $|1\rangle$, and $|2\rangle$ states. Depending on the parity, there are different probabilities of the transmon being mapped on the states indicated by colored arrows in Fig. 11(a), which we call emission probabilities. Between two consecutive runs, the hidden parity can change or stay the same with fixed probabilities $t_{\mathrm{rep}}\Gamma_{ij}$ where t_{rep} is the repetition time and Γ_{ij} [with $i,j = \{$"even" (e), "odd" (o)$\}$] are the transition rates illustrated by black arrows in Fig. 11(a). In the model, we allow for different Γ_{eo} and Γ_{oe}, which in turn fix Γ_{oo} and Γ_{ee}. The calibration points for the $|0\rangle$, $|1\rangle$, and $|2\rangle$ states are obtained by preparing those states followed by a measurement [see Fig. 11(b)]. Each *IQ* histogram for the prepared states ($|0\rangle$, $|1\rangle$, and $|2\rangle$) is well described by sums of three Gaussian probability distributions (one of the three Gaussians clearly dominates for each state, but we consider that our calibration points are slightly mixed due to residual excitation as well as relaxation). The means and covariances of the dominant Gaussians corresponding to $|0\rangle$, $|1\rangle$, and $|2\rangle$, respectively, fix the probability distributions of the Gaussian HMM. The free parameters of the HMM are the emission probabilities of the "even" and "odd" parities (the probabilities to measure each state given a parity) as well as Γ_{eo} and Γ_{oe}. These parameters are determined by a likelihood fit of the HMM to the data using the *hmmlearn* package [67].

As outcomes of the HMM fit, we get the assigned parities for each run and the transition probabilities, from which $\tau_p^e = (\Gamma_{\mathrm{eo}})^{-1}$ and $\tau_p^o = (\Gamma_{\mathrm{oe}})^{-1}$ can be calculated with the known repetition time of the sequence. Figures 11(c) and 11(d) show the assigned parities as a function of time; here the assigned states are based on a Gaussian classifier yielding the most likely state for any point in the *IQ* plane [see colors in Fig. 11(b)]. We find that generally the "even" ("odd") parity is associated with the $|0\rangle$ ($|1\rangle$) state. The histograms of the *IQ* data selected on the "even" and "odd" parity are shown in Figs. 11(e) and 11(f). The overlap of the emission probability distributions of the two parities is $1 - F_p$ with F_p being the parity-measurement fidelity. To check the HMM methodology for consistency, we compared it with the results for the parity-switching time based on a fit to the power spectral density of the assigned states (see Supplemental Material [49]).

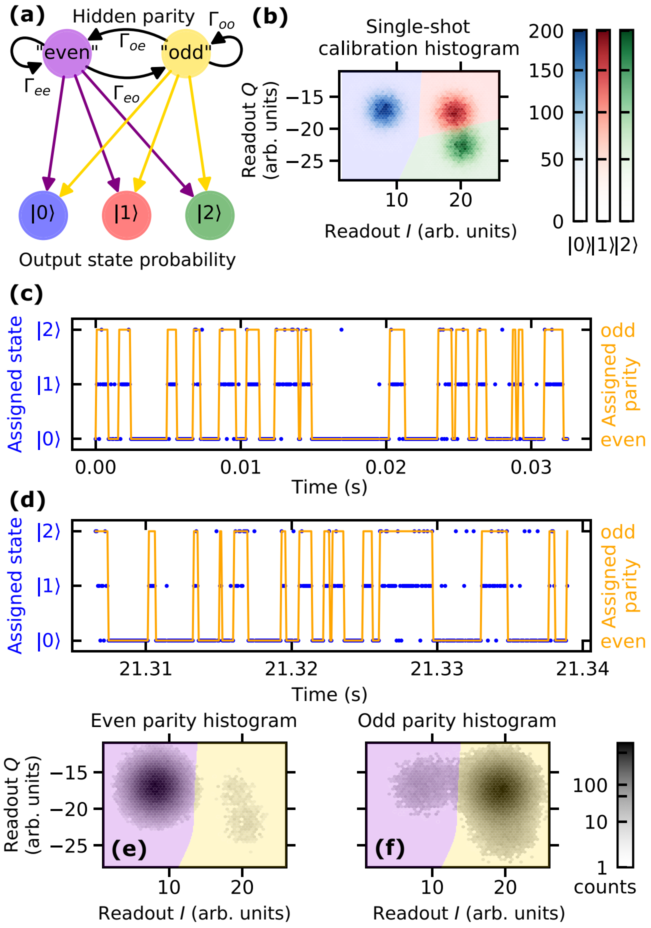

FIG. 11. (a) Diagram illustrating the Gaussian mixture hidden Markov model. The parity state changes with certain (fixed) probabilities between runs. Both parities have different state probabilities, which correspond to different weights in a Gaussian mixture for the output probabilities. (b) Histogram of calibration points for the different prepared states directly preceding the parity measurement run. The colors show the most likely state in each region based on a Gaussian classifier. (c),(d) Assigned states from the Gaussian classifier and assigned parities from the HMM fit for the first 400 measurements at the beginning and the end of the parity measurement run comprising $2^{18} = 262144$ measurements. (e),(f) Histograms of the output voltages conditioned on the assigned parity. The colors show the most likely parity in each region based on a Gaussian classifier.

We filter our data based on Ramsey measurements before and after each parity measurement sequence: The splitting δf_{ij} between "even" and "odd" transmon frequencies has to match $t_w = (2\delta f_{ij})^{-1}$, and we reject data in which the transmon frequencies drifted during the time of the parity-measurement sequence. Moreover, we ensured that t_w is small compared to T_2^* and T_1.

APPENDIX G: MODELING THE CONTRIBUTIONS TO THE PARITY-SWITCHING TIME

We discussed the theoretical model for the parity-switching time in Sec. IV A of the main text. Here, we present explicit expressions for the rates associated with PAPS and NUPS contributions in Eqs. (2)–(6). The parity-switching time measurements have been performed at the lower sweet spot of the split-transmon device ($\Phi = \Phi_0/2$), where the gap difference is larger than the qubit energy transition, *i.e.*, $f_{\delta\Delta} > f_{01}$ (denoted as case II in Ref. [37]) with $f_{\delta\Delta} = (\Delta_B - \Delta_T)/h$. In this situation, quasiparticles accumulate in the lower-gap electrode at energies close to its gap due to relaxation (via phonon emission) and suppressed tunneling into the higher-gap electrode (because of the energy difference $f_{\delta\Delta} - f_{01} > 0$), see Ref. [37].

As in the reference, we describe the quasiparticle dynamics in each superconducting electrode via rate equations for their density, see also Appendix E of Ref. [35] and Sec. III.D of the Supplemental Material to Ref. [36]. The equations are written in terms of the dimensionless quantities x_B and x_T, obtained normalizing the quasiparticle density in electrode $\alpha = \{B, T\}$ by the Cooper pair density $n^\alpha_{\mathrm{Cp}} = 2\nu_0\Delta_\alpha$ (with $\nu_0 \approx 0.73 \times 10^{47}\,\mathrm{J}^{-1}\mathrm{m}^{-3}$ the single spin density of states of aluminum at the Fermi level and Δ_α the superconducting gap),

$$\frac{dx_B}{dt} = g^B - s_B x_B - r^B x_B^2 + \delta\bar{\Gamma}^{\mathrm{T}} x_T - \delta\bar{\Gamma}^B x_B, \tag{G1}$$

$$\frac{dx_T}{dt} = g^{\mathrm{T}} - s_{\mathrm{T}} x_T - r^{\mathrm{T}} x_T^2 - \bar{\Gamma}^{\mathrm{T}} x_T + \bar{\Gamma}^B x_B, \tag{G2}$$

where $\delta = \Delta_T/\Delta_B$. In the right-hand sides of Eqs. (G1) and (G2), g^α, $\alpha = \{T, B\}$, describe quasiparticle generation, and the terms proportional to s_α and r^α account for quasiparticle trapping and recombination, respectively; for the recombination rate, we use the values $r^T = r^B = 1/(160\ \mathrm{ns})$ [37,59]. Finally, the terms proportional to

$$\bar{\Gamma}^\alpha = (1 - p_1)\left(\bar{\Gamma}^\alpha_{00} + \bar{\Gamma}^\alpha_{01}\right) + p_1\left(\bar{\Gamma}^\alpha_{11} + \bar{\Gamma}^\alpha_{10}\right) \tag{G3}$$

account for the tunneling of quasiparticles initially located in electrode α ($\alpha = \{T, B\}$) into the other electrode, where p_1 is the occupation probability of the excited state of the qubit. Note that in writing the first factor on the right-hand side in the form $(1 - p_1) = p_0$ we implicitly assume that the occupations of higher levels can be ignored; it was estimated in the Supplemental Material to Ref. [36] that for high p_1 taking the occupation of second excited state into consideration could lead to corrections of the order of several percent, so we neglect this possibility here. In our notation for NUPS [see, for instance, Eqs. (4)–(6) in the main text], $\tilde{\Gamma}^\alpha_{ij} x_\alpha$ represents the quasiparticle-tunneling-induced transition rate for the qubit from the initial logical state i to the final state j ($i, j = \{0, 1\}$). The barred rates $\bar{\Gamma}_{ij}$ are obtained dividing $\tilde{\Gamma}_{ij}$ by the Cooper-pair number in the low-gap electrode, i.e., $\bar{\Gamma}^\alpha = \tilde{\Gamma}^\alpha/(n^T_{\mathrm{Cp}}\mathcal{V}_T)$, where $\mathcal{V}_{\mathrm{T}} \simeq 3400\ \mu\mathrm{m}^3$ is the volume of the low-gap electrode; this normalization is at the origin of the factors δ appearing in Eq. (G1). In comparing Eqs. (G1) and (G2) to the model of Ref. [37] [see Eqs. (11)–(13) there], we note that here the terms $-s_\alpha x_\alpha$ in the right-hand side account for trapping (cf. Sec. IV.D in Ref. [37]) and we additionally assume quasiequilibrium quasiparticle distributions in both electrodes, having temperature coinciding with the phonon temperature, but allowing for different effective chemical potentials in the two electrodes. This assumption enables us to use a single equation for $x_T = x_{T<} + x_{T>}$ obtained by summing Eqs. (12) and (13) of Ref. [37] (the rates from the top electrode are defined so to obtain $\bar{\Gamma}^T_{ij} x_T = \bar{\Gamma}^{T<}_{ij} x_{T<} + \bar{\Gamma}^{T>}_{ij} x_{T>}$).

For the modeling of the parity-switching time, we are interested in the steady-state values of the quasiparticle densities in the two electrodes ($dx_B/dt = dx_T/dt = 0$). Assuming $\delta\bar{\Gamma}_B + s_B \gg r^B x_B$, we can neglect recombination in the bottom electrode in Eq. (G1), and then we can express the steady-state value of x_B in terms of x_T,

$$\begin{aligned} x_B &= \frac{g^B/\delta + \left[p_0\left(\bar{\Gamma}^T_{00} + \bar{\Gamma}^T_{01}\right) + p_1\left(\bar{\Gamma}^T_{11} + \bar{\Gamma}^T_{10}\right)\right] x_T}{p_0\left(\bar{\Gamma}^B_{00} + \bar{\Gamma}^B_{01}\right) + p_1\left(\bar{\Gamma}^B_{11} + \bar{\Gamma}^B_{10}\right) + s_B/\delta} \\ &\approx \frac{g^B/\delta + \left(\bar{\Gamma}^T_{00} + p_1\bar{\Gamma}^T_{10}\right) x_T}{\bar{\Gamma}^B_{00} + p_0\bar{\Gamma}^B_{01} + p_1\bar{\Gamma}^B_{10} + s_B/\delta}. \end{aligned} \tag{G4}$$

The approximate expression in the second line of Eq. (G4) is obtained noticing that parity-switching rates for a transmon qubit are independent of the logical state of the qubit at the leading order in $E_{\mathrm{J}}/E_{\mathrm{C}}$ [37,77], i.e., $\bar{\Gamma}^\alpha_{00} \approx \bar{\Gamma}^\alpha_{11}$, and neglecting the contribution of transitions exciting the qubit for quasiparticles initially located in the low-gap (top) electrode, since $\bar{\Gamma}^T_{01} \ll \bar{\Gamma}^T_{00}, \bar{\Gamma}^T_{10}$ (the rates are discussed in more detail later in this Appendix). This strong inequality also justifies neglecting terms proportional to x_T in qubit's excitation rates [see Eq. (5) in the main text]. Substituting Eq. (G4) into Eq. (G2), the steady-state density in the top electrode x_T is obtained by solving a quadratic equation, yielding the result

$$x_T = \frac{\sqrt{\tilde{s}^2 + 4\tilde{g}r^T} - \tilde{s}}{2r^T}, \tag{G5}$$

where for notational convenience, we introduced an effective trapping rate $\tilde{s}$

$$\tilde{s} = s_T + s_B \frac{p_0\left(\bar{\Gamma}^T_{00} + \bar{\Gamma}^T_{01}\right) + p_1\left(\bar{\Gamma}^T_{11} + \bar{\Gamma}^T_{10}\right)}{s_B + \delta\left[p_0\left(\bar{\Gamma}^B_{00} + \bar{\Gamma}^B_{01}\right) + p_1\left(\bar{\Gamma}^B_{11} + \bar{\Gamma}^B_{10}\right)\right]}$$
$$\approx s_T + s_B \frac{\bar{\Gamma}^T_{00} + p_1\bar{\Gamma}^T_{10}}{s_B + \delta\left[\bar{\Gamma}^B_{00} + p_0\bar{\Gamma}^B_{01} + p_1\bar{\Gamma}^B_{10}\right]}, \tag{G6}$$

and generation rate $\tilde{g}$

$$\tilde{g} = g^T + \frac{g^B}{\delta}\left(1 - \frac{s_B}{\delta\left[p_0\left(\bar{\Gamma}^B_{00} + \bar{\Gamma}^B_{01}\right) + p_1\left(\bar{\Gamma}^B_{11} + \bar{\Gamma}^B_{10}\right)\right] + s_B}\right)$$
$$\approx g^T + \frac{g^B}{\delta}\left(1 - \frac{s_B}{\delta\left[\bar{\Gamma}^B_{00} + p_0\bar{\Gamma}^B_{01} + p_1\bar{\Gamma}^B_{10}\right] + s_B}\right). \tag{G7}$$

The generation rates in the two electrodes originate from pair breaking by high-frequency photons with rate g^{PAPS} and by thermal phonons,

$$g^B/\delta = g^{\mathrm{PAPS}}, \; g_T = g^{\mathrm{PAPS}} + 2\pi r^T \frac{k_{\mathrm{B}}T}{\Delta_T} e^{-2\Delta_T/k_{\mathrm{B}}T} \tag{G8}$$

where thermal phonons generation in the high-gap (bottom) electrode is neglected for consistency with the approximation ignoring recombination there (alternatively, once the parameters are determined from the experimental data, one can check if the thermal phonon generation term is small compared the the photon pair-breaking one, which independently justifies ignoring the former). The photon-assisted generation rate is computed by dividing the photon-assisted tunneling rates Γ^{PAPS} [37,54] by the Cooper-pair number in the low-gap electrode,

$$g^{\mathrm{PAPS}} = \frac{\Gamma^{\mathrm{PAPS}}}{n^T_{\mathrm{Cp}}\mathcal{V}_T} \approx \frac{\Gamma^{\mathrm{ph}}_{00} + p_0\Gamma^{\mathrm{ph}}_{01} + p_1\Gamma^{\mathrm{ph}}_{10}}{2\nu_0\mathcal{V}_T\Delta_T}. \tag{G9}$$

The (inverse) parity-switching time can be expressed summing all the rates associated with quasiparticle tunneling, reading

$$\tau_P^{-1} = \Gamma^{\mathrm{PAPS}} + \left[p_0\left(\tilde{\Gamma}^B_{00} + \tilde{\Gamma}^B_{01}\right) + p_1\left(\tilde{\Gamma}^B_{11} + \tilde{\Gamma}^B_{10}\right)\right]x_B + \left[p_0\left(\tilde{\Gamma}^T_{00} + \tilde{\Gamma}^T_{01}\right) + p_1\left(\tilde{\Gamma}^T_{11} + \tilde{\Gamma}^T_{10}\right)\right]x_T$$
$$\approx \Gamma^{\mathrm{PAPS}} + \left(\tilde{\Gamma}^B_{00} + p_1\tilde{\Gamma}^B_{10} + p_0\tilde{\Gamma}^B_{01}\right)x_B + \left(\tilde{\Gamma}^T_{00} + p_1\tilde{\Gamma}^T_{10}\right)x_T$$
$$= \left(2 - \frac{s_B}{\delta\left[\bar{\Gamma}^B_{00} + p_0\bar{\Gamma}^B_{01} + p_1\bar{\Gamma}^B_{10}\right] + s_B}\right) \times \left[\Gamma^{\mathrm{PAPS}} + (\tilde{\Gamma}^T_{00} + p_1\tilde{\Gamma}^T_{10})x_T\right]. \tag{G10}$$

The calculation of the quasiparticle rates $\tilde{\Gamma}^{\alpha}_{ij}$ and $\Gamma^{\mathrm{ph}}_{ij}$ can be performed using Fermi's Golden rule, as extensively discussed in the literature, see, for instance, Refs. [36,37,77,78]. Below, we report the results for the rates entering τ_P^{-1} under the assumption of quasiequilibrium distributions in the two electrodes; the detailed derivation of the quasiparticle rates in the presence of Fraunhofer effect will be given elsewhere. First, we consider the relaxation and parity-switching tunneling rates for quasiparticles initially located in the top electrode:

$$\tilde{\Gamma}^T_{10} = \frac{8E^0_{\mathrm{J}\Sigma}}{h}\sqrt{\frac{E_{\mathrm{C}}}{8E_{\mathrm{J}}}}\sqrt{\frac{2\Delta_T}{\pi k_{\mathrm{B}}T}}\,\mathrm{Exp}\left[-\frac{h(f_{\delta\Delta} - f_{01})}{2k_{\mathrm{B}}T}\right]\left\{\gamma_+ K_0\left[\frac{h|f_{\delta\Delta} - f_{01}|}{2k_{\mathrm{B}}T}\right] + \left(\gamma_- + \frac{\gamma_+}{2}\right)\frac{h|f_{\delta\Delta} - f_{01}|}{2\bar{\Delta}}K_1\left[\frac{h|f_{\delta\Delta} - f_{01}|}{2k_{\mathrm{B}}T}\right]\right\}, \tag{G11}$$

$$\tilde{\Gamma}^T_{00} = \frac{8E^0_{\mathrm{J}\Sigma}}{h}\sqrt{\frac{2\Delta_T}{\pi k_{\mathrm{B}}T}}\,\mathrm{Exp}\left[-\frac{hf_{\delta\Delta}}{2k_{\mathrm{B}}T}\right]\left\{\gamma_- K_0\left[\frac{h|f_{\delta\Delta}|}{2k_{\mathrm{B}}T}\right] + \left(\gamma_+ + \frac{\gamma_-}{2}\right)\frac{h|f_{\delta\Delta}|}{2\bar{\Delta}}K_1\left[\frac{h|f_{\delta\Delta}|}{2k_{\mathrm{B}}T}\right]\right\}, \tag{G12}$$

where E_{J} and f_{01} are the Josephson energy and the frequency of the qubit at the lower sweet spot in the presence of the parallel field, K_n are modified Bessel functions of the second kind, and $E^0_{\mathrm{J}\Sigma} = E_{\mathrm{J}a}(B_\parallel = 0) + E_{\mathrm{J}b}(B_\parallel = 0)$. The remaining rates are obtained from the ones given in Eqs. (G11) and (G12) with the following substitutions:

$$\tilde{\Gamma}^T_{01} = \tilde{\Gamma}^T_{10}(f_{01} \to -f_{01}) \tag{G13}$$

$$\tilde{\Gamma}^B_{10} = \sqrt{\frac{\Delta_B}{\Delta_T}}\tilde{\Gamma}^T_{10}(f_{\delta\Delta} \to -f_{\delta\Delta}), \tag{G14}$$

$$\tilde{\Gamma}^B_{00} = \sqrt{\frac{\Delta_B}{\Delta_T}}\,\mathrm{Exp}\left[\frac{hf_{\delta\Delta}}{k_{\mathrm{B}}T}\right]\tilde{\Gamma}^T_{00}, \tag{G15}$$

$$\tilde{\Gamma}^B_{01} = \sqrt{\frac{\Delta_B}{\Delta_T}}\,\mathrm{Exp}\left[\frac{-h(f_{01} - f_{\delta\Delta})}{k_{\mathrm{B}}T}\right]\tilde{\Gamma}^T_{10}. \tag{G16}$$

The transformations in Eqs. (G14) and (G15) exploit the symmetry of the rates and are equivalent to exchanging the role of the two electrodes $B \leftrightarrow T$, while Eq. (G16) follows from the detailed balance principle. The weights in the curly brackets of Eqs. (G11) and (G12)

$$\gamma_{\pm}=\frac{2 \pm (z_{-}+\alpha_{\mathrm{JJ},0} z_{+})}{4} \tag{G17}$$

accounts for the interference effects related to the SQUID interferometer as well as the Fraunhofer effect: $\alpha_{\mathrm{JJ},0} = \alpha_{\mathrm{JJ}}(B_{\parallel} = 0) = (E_{\mathrm{J}a} - E_{\mathrm{J}b})/(E_{\mathrm{J}a} + E_{\mathrm{J}b})$ is the split-transmon asymmetry parameter at zero parallel field, while $z_{\pm} = \mathrm{sinc}(B_{\parallel}/B_{\Phi_{0,a}}) \pm \mathrm{sinc}(B_{\parallel}/B_{\Phi_{0,b}})$. For comparison, the rates for a single-junction transmon correspond to the case $\alpha_{\mathrm{JJ},0} = 1$; if we further consider zero parallel magnetic field, we have $\{\gamma_{+}, \gamma_{-}\} = \{1, 0\}$.

We can present the photon-assisted tunneling rates $\Gamma^{\mathrm{ph}}_{ij}$ in a similar way. For simplicity, we consider monochromatic radiation with frequency $f_{\nu} > (\Delta_B + \Delta_T)/h$ to allow for Cooper-pair breaking. The rates can be expressed as

$$\Gamma^{\mathrm{ph}}_{00} = \Gamma_{\nu} \frac{g_{\Sigma} \Delta_B}{8e^2} \left[\gamma_{-} S^{+}_{\mathrm{ph}}\left(\frac{hf_{\nu}}{\Delta_B}, \delta\right) + \gamma_{+} S^{-}_{\mathrm{ph}}\left(\frac{hf_{\nu}}{\Delta_B}, \delta\right)\right] \tag{G18}$$

$$\Gamma^{\mathrm{ph}}_{10} = \Gamma_{\nu} \frac{g_{\Sigma} \Delta_B}{8e^2} \sqrt{\frac{E_{\mathrm{C}}}{8E_{\mathrm{J}}}} \left[\gamma_{+} S^{+}_{\mathrm{ph}}\left(\frac{f_{\nu} + f_{01}}{\Delta_B/h}, \delta\right) + \gamma_{-} S^{-}_{\mathrm{ph}}\left(\frac{f_{\nu} + f_{01}}{\Delta_B/h}, \delta\right)\right] \tag{G19}$$

$$\Gamma^{\mathrm{ph}}_{01} = \Gamma_{\nu} \frac{g_{\Sigma} \Delta_B}{8e^2} \sqrt{\frac{E_{\mathrm{C}}}{8E_{\mathrm{J}}}} \left[\gamma_{+} S^{+}_{\mathrm{ph}}\left(\frac{f_{\nu} - f_{01}}{\Delta_B/h}, \delta\right) + \gamma_{-} S^{-}_{\mathrm{ph}}\left(\frac{f_{\nu} - f_{01}}{\Delta_B/h}, \delta\right)\right] \tag{G20}$$

where $g_{\Sigma} \approx 8 g_k E^{0}_{\mathrm{J}\Sigma}(\Delta_B + \Delta_T)/(2\Delta_B \Delta_T)$ is the total tunnel conductance of the SQUID in the normal state, $g_k = e^2/h$ is the conductance quantum, Γ_{ν} is the dimensionless photon rate that accounts for the coupling strength between transmon and pair-breaking photons, and the photon spectral densities read [37]

$$\begin{aligned} S^{\pm}_{\mathrm{ph}}(x,z) &= \theta(x-1-z) \int_{1}^{x-z} dy \frac{y(x-y) \pm z}{\sqrt{y^2-1}\sqrt{(x-y)^2 - z^2}} \\ &= \theta(x-1-z) \left\{ \sqrt{x^2-(z-1)^2} E\left[\sqrt{\frac{x^2-(z+1)^2}{x^2-(z-1)^2}}\right] \right. \\ &\quad \left. -2z \frac{1 \mp 1}{\sqrt{x^2-(z-1)^2}} K\left[\sqrt{\frac{x^2-(z+1)^2}{x^2-(z-1)^2}}\right] \right\} \end{aligned} \tag{G21}$$

with E and K complete elliptic integrals of the second and first kind, respectively.

We note that all the rates, being expressed in terms of the conductance g_{Σ}, are calculated at leading order in the tunneling transmission probability. This means, in particular, that we are ignoring effects comparable in magnitude to those of the Josephson harmonics, which can introduce corrections at most at the percent level, see Appendix C and Ref. [52]. Given the limited accuracy of time-domain measurements, this approach is sufficient for our purposes.

Finally, let us comment on the data-fitting procedure. We base values for E_{J}, E_{C}, and f_{01} on the fitting of the spectroscopic data (Appendices C and D); the occupation probability p_1 are estimated based on the single-shot parity outcomes and the measured relaxation times (see Fig. 3 and Appendix H). We estimate the smaller gap Δ_T based on modeling the temperature dependence of T_1 (see Appendix I). That leaves as unknown parameters the gap difference, the photon frequency, the trapping rates, and the dimensionless photon rate. The values used in calculating the theoretical curves in Figs. 4 and 5 are $\delta\Delta/h = 5.48$ GHz, $f_{\nu} = 119$ GHz, $s_B = s_T = 3.39$ Hz, and $\Gamma_{\nu} = 1.71 \times 10^{-8}$.

APPENDIX H: MODELING THE TEMPERATURE DEPENDENCE OF THE EXCITED-STATE POPULATION

In our model, the parity switching time is parametrically expressed in terms of the populations of the ground and first excited state of the transmon (see Appendix G). The population of the excited state of the qubit is given by

$$p_1 = \frac{\Gamma^{\mathrm{ee}}_{01} + \Gamma^{\mathrm{eo}}_{01}}{\Gamma^{\mathrm{ee}}_{01} + \Gamma^{\mathrm{eo}}_{01} + \Gamma^{\mathrm{ee}}_{10} + \Gamma^{\mathrm{ee}}_{10}} = \left(\Gamma^{\mathrm{ee}}_{01} + \Gamma^{\mathrm{eo}}_{01}\right) T_1, \tag{H1}$$

where $\Gamma^{\mathrm{ee}}_{10}$, and $\Gamma^{\mathrm{ee}}_{01}$ are the parity-preserving (thus not associated with quasiparticles) qubit' relaxation and excitation rates, respectively. For terms changing the parity, we identity the rates adding NUPS and PAPS contributions, i.e., $\Gamma^{\mathrm{eo}}_{10} = \Gamma^{\mathrm{ph}}_{10} + \Gamma^{\mathrm{qp}}_{10}/p_1$ and $\Gamma^{\mathrm{eo}}_{01} = \Gamma^{\mathrm{ph}}_{01} + \Gamma^{\mathrm{qp}}_{01}/p_0$ [cf. Eqs. (5) and (6)]. In the temperature regime for the parity-switching time measurements, the lifetime of the qubit is mainly limited by dielectric losses $T_1 \approx 1/(\Gamma^{\mathrm{ee}}_{10} + \Gamma^{\mathrm{ee}}_{01})$. Indeed, the maximum qubit's lifetime is of the order of 10 µs (see Appendix I), which is more than an order of magnitude shorter than the parity lifetime. Assuming that the parity-preserving rates satisfy the detailed balance principle, i.e., $\Gamma^{\mathrm{ee}}_{01} = \Gamma^{\mathrm{ee}}_{10} e^{-hf_{01}/k_{\mathrm{B}}T}$, we can write

$$p_1 \approx T_1 \Gamma^{\mathrm{eo}}_{01} + \frac{\exp(-hf_{01}/k_{\mathrm{B}}T)}{1 + \exp(-hf_{01}/k_{\mathrm{B}}T)}. \tag{H2}$$

In the experimental protocol for determining the parity-switching time, the qubit's parity is mapped onto the qubit's logical state, with the convention e → 0 and o → 1. After the mapping, the qubit's state is not reset to zero, rather there is a waiting time equal to five times T_1. As a result, the qubit's excited-state population relaxes exponentially from $p_1 = 0$ (for even assignment) or $p_1 = 1$ (for odd assignment) to the steady-state value p_1 of Eq. (H1). Integrating the rate equation for the qubit's excited-state population over the waiting time $5T_1$, we obtain the average excited-state population for the two parity assignments

$$\overline{p}_1^{\rm e} \approx 0.8\,p_1, \overline{p}_1^{\rm o} \approx 0.2 + 0.8\,p_1. \tag{H3}$$

The analysis of the hidden Markov model, combined with the considerations on the parity assignment, allows us to determine an average population of the excited state during the measurements of the parity-switching rates [points in Figs. 5(e) and 5(f)]. Motivated by the considerations made above, we use the following semiphenomenological expression

$$p_1^{\rm fit} = \frac{a}{1 + {\rm Exp}[-hf_{01}/k_{\rm B}T]} + b\,\frac{{\rm Exp}[-hf_{01}/k_{\rm B}T]}{1 + {\rm Exp}[-hf_{01}/k_{\rm B}T]} \tag{H4}$$

and we perform a two-parameter fit (a, b) to the data [solid curves in Figs. 5(e) and 5(f)]. The parameter a quantifies the average excited-state population at low temperatures $T \ll hf_{01}/k_{\rm B}$; for even assignment, it is in the range of a few percent while for odd assignment is around 20% [see the considerations leading to Eq. (H3)]. The prefactor of the last term in Eq. (H4) turns out to be in the range of 0.8 to 1.3, in reasonable agreement with our interpretation.

APPENDIX I: TEMPERATURE DEPENDENCE OF THE QUBIT RELAXATION TIME

As mentioned in Appendix H, the qubit relaxation time T_1 is much shorter than the parity-switching time at the base temperature of the dilution refrigerator, suggesting that T_1 is limited by decay processes unrelated to quasiparticle tunneling, such as dielectric losses; we model the latter as a two-level-system bath. At low temperatures, $T \ll hf_{01}/k_{\rm B}$, the qubit's relaxation time is approximately the inverse of the parity-conserving relaxation rate, $T_1 \approx 1/\Gamma_{10}^{\rm ee}$, see Appendix H; this quantity is an unknown function of the parallel magnetic field. Upon increasing the temperature $T \lesssim hf_{01}/k_{\rm B}$, the qubit lifetime decreases due to the non-negligible qubit excitation rate caused by the TLS bath. Moreover, the quasiparticle density increases exponentially with the phonon temperature; thus, the qubit's relaxation time is eventually limited by quasiparticle tunneling above a crossover temperature; we assume this temperature to be sufficiently high so that deviations of the quasiparticle distribution from thermal equilibrium due to, e.g., photon pair breaking can be ignored (see the discussion at the end of this Appendix).

As in previous works [77,78], to capture the temperature evolution of the qubit's relaxation time we sum the thermal quasiparticle decoherence rate ($T_{1,\rm qp}^{-1}$) and the contribution of the dielectric losses,

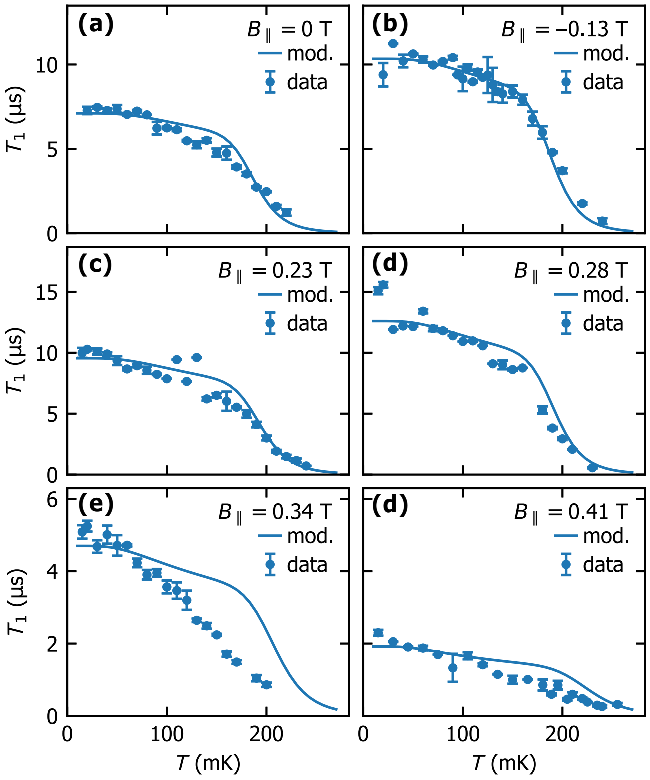

FIG. 12. Qubit lifetime vs temperature for different values of the in-plane magnetic field. Points are the experimental data, continuous curves are given by Eq. (I1) and are obtained using $\Delta_B/h = 59.48$ GHz, $\Delta_T/h = 54$ GHz, and the spectroscopic parameters estimated in Appendices C and D. The parity preserving relaxation rate used in the plot is $\Gamma_{10}^{\rm ee} =$ (a) 141 kHz, (b) 97 kHz, (c) 105 kHz, (d) 79 kHz, (e) 213 kHz, (f) 521 kHz. The dependence of the superconducting gaps on the magnetic field has not been included.

$$T_1(T) = \left\{\Gamma_{10}^{\rm ee}\left[1 + \exp\left(-\frac{hf_{01}}{k_{\rm B}T}\right)\right] + T_{1,\rm qp}^{-1}(T)\right\}^{-1}. \tag{I1}$$

The relaxation rate due to thermal quasiparticles alone is

$$T_{1,\rm qp}^{-1} = \left(\tilde{\Gamma}_{10}^{B} x_B^{\rm th} + \tilde{\Gamma}_{10}^{T} x_T^{\rm th}\right)[1 + \exp(-hf_{01}/k_{\rm B}T)], \tag{I2}$$

where

$$x_\alpha^{\rm th} = \sqrt{\frac{2\pi k_{\rm B}T}{\Delta_\alpha}}\exp\left[-\frac{\Delta_\alpha}{k_{\rm B}T}\right] \tag{I3}$$

is the thermal quasiparticle density in the electrode $\alpha = \{T, B\}$. In Eq. (I2), the relaxation rate for quasiparticles tunneling from the top to the bottom electrode $\tilde{\Gamma}_{10}^{T}$ is given by Eq. (G11), the corresponding rate for quasiparticles initially located in the bottom electrode is simply obtained exchanging $\Delta_B \leftrightarrow \Delta_T$ in Eq. (G11) in agreement with Eq. (G14). The exponential factor in the square bracket of Eq. (I2) accounts for qubit's excitation rates, according to the detailed balance principle.

To check that the thermal equilibrium assumption for quasiparticles is justified in fitting the T_1 data, we proceed as follows: we start by noticing that the thermal quasiparticle contribution becomes relevant at temperature approximately 170 mK above which T_1 decreases markedly faster with temperature, see Fig. 12. At that temperature, the thermal phonon generation rate is given by $r^\alpha (x_\alpha^{\text{th}})^2$, cf. the last term in Eq. (G8); for the low-gap (top) electrode, this rate is about 1.5×10^{-7} Hz. The thermal phonon generation rate should be compared with g^{PAPS} of Eq. (G9), which we estimate to be at most of order 3.7×10^{-8} Hz (cf. Fig. 4); therefore, nonequilibrium generation by pair-breaking photons can be ignored when analyzing the T_1 data. Conversely, we conclude that in our experiment at temperatures below about 150 mK the generation by thermal phonons plays essentially no role in the temperature dependence of τ_p; in fact, in Figs. 5(a) and 5(b) we see a steeper decline in τ_p beginning at that temperature.

[1] M. Kjaergaard, M. E. Schwartz, J. Braumüller, P. Krantz, J. I.-J. Wang, S. Gustavsson, and W. D. Oliver, Superconducting qubits: Current state of play, Annu. Rev. Condens. Matter Phys. **11**, 369 (2020).

[2] C. Wang, C. Axline, Y. Y. Gao, T. Brecht, Y. Chu, L. Frunzio, M. H. Devoret, and R. J. Schoelkopf, Surface participation and dielectric loss in superconducting qubits, Appl. Phys. Lett. **107**, 162601 (2015).

[3] J. M. Martinis, Surface loss calculations and design of a superconducting transmon qubit with tapered wiring, npj Quantum Inf. **8**, 26 (2022).

[4] A. D. Córcoles, J. M. Chow, J. M. Gambetta, C. Rigetti, J. R. Rozen, G. A. Keefe, M. Beth Rothwell, M. B. Ketchen, and M. Steffen, Protecting superconducting qubits from radiation, Appl. Phys. Lett. **99**, 181906 (2011).

[5] J. Koch, T. M. Yu, J. Gambetta, A. A. Houck, D. I. Schuster, J. Majer, A. Blais, M. H. Devoret, S. M. Girvin, and R. J. Schoelkopf, Charge-insensitive qubit design derived from the Cooper pair box, Phys. Rev. A **76**, 042319 (2007).

[6] A. P. M. Place, L. V. H. Rodgers, P. Mundada, B. M. Smitham, M. Fitzpatrick, Z. Leng, A. Premkumar, J. Bryon, A. Vrajitoarea, S. Sussman *et al.*, New material platform for superconducting transmon qubits with coherence times exceeding 0.3 milliseconds, Nat. Commun. **12**, 1779 (2021).

[7] K. Serniak, M. Hays, G. de Lange, S. Diamond, S. Shankar, L. D. Burkhart, L. Frunzio, M. Houzet, and M. H. Devoret, Hot nonequilibrium quasiparticles in transmon qubits, Phys. Rev. Lett. **121**, 157701 (2018).

[8] M. McEwen, L. Faoro, K. Arya, A. Dunsworth, T. Huang, S. Kim, B. Burkett, A. Fowler, F. Arute, J. C. Bardin *et al.*, Resolving catastrophic error bursts from cosmic rays in large arrays of superconducting qubits, Nat. Phys. **18**, 107 (2022).

[9] P. M. Harrington, M. Li, M. Hays, W. Van De Pontseele, D. Mayer, H. D. Pinckney, F. Contipelli, M. Gingras, B. M. Niedzielski, H. Stickler, J. L. Yoder, M. E. Schwartz, J. A. Grover, K. Serniak, W. D. Oliver, and J. A. Formaggio, Synchronous detection of cosmic rays and correlated errors in superconducting qubit arrays, arXiv:2402.03208.

[10] R.-P. Riwar, A. Hosseinkhani, L. D. Burkhart, Y. Y. Gao, R. J. Schoelkopf, L. I. Glazman, and G. Catelani, Normal-metal quasiparticle traps for superconducting qubits, Phys. Rev. B **94**, 104516 (2016).

[11] S. Gustavsson, F. Yan, G. Catelani, J. Bylander, A. Kamal, J. Birenbaum, D. Hover, D. Rosenberg, G. Samach, A. P. Sears, S. J. Weber, J. L. Yoder, J. Clarke, A. J. Kerman, F. Yoshihara, Y. Nakamura, T. P. Orlando, and W. D. Oliver, Suppressing relaxation in superconducting qubits by quasiparticle pumping, Science **354**, 1573 (2016).

[12] L. Sun, L. DiCarlo, M. D. Reed, G. Catelani, L. S. Bishop, D. I. Schuster, B. R. Johnson, G. A. Yang, L. Frunzio, L. Glazman, M. H. Devoret, and R. J. Schoelkopf, Measurements of quasiparticle tunneling dynamics in a band-gap-engineered transmon qubit, Phys. Rev. Lett. **108**, 230509 (2012).

[13] R.-P. Riwar and G. Catelani, Efficient quasiparticle traps with low dissipation through gap engineering, Phys. Rev. B **100**, 144514 (2019).

[14] P. Kamenov, T. DiNapoli, M. Gershenson, and S. Chakram, Suppression of quasiparticle poisoning in transmon qubits by gap engineering, arXiv:2309.02655.

[15] M. McEwen *et al.*, Resisting high-energy impact events through gap engineering in superconducting qubit arrays, arXiv:2402.15644.

[16] F. Henriques, F. Valenti, T. Charpentier, M. Lagoin, C. Gouriou, M. Martínez, L. Cardani, M. Vignati, L. Grünhaupt, D. Gusenkova, J. Ferrero, S. T. Skacel, W. Wernsdorfer, A. V. Ustinov, G. Catelani, O. Sander, and I. M. Pop, Phonon traps reduce the quasiparticle density in superconducting circuits, Appl. Phys. Lett. **115**, 212601 (2019).

[17] V. Iaia, J. Ku, A. Ballard, C. P. Larson, E. Yelton, C. H. Liu, S. Patel, R. McDermott, and B. L. T. Plourde, Phonon downconversion to suppress correlated errors in superconducting qubits, Nat. Commun. **13**, 6425 (2022).

[18] X. Pan, Y. Zhou, H. Yuan, L. Nie, W. Wei, L. Zhang, J. Li, S. Liu, Z. H. Jiang, G. Catelani, L. Hu, F. Yan, and D. Yu, Engineering superconducting qubits to reduce quasiparticles and charge noise, Nat. Commun. **13**, 7196 (2022).

[19] R. T. Gordon, C. E. Murray, C. Kurter, M. Sandberg, S. A. Hall, K. Balakrishnan, R. Shelby, B. Wacaser, A. A. Stabile, J. W. Sleight, M. Brink, M. B. Rothwell, K. P. Rodbell, O. Dial, and M. Steffen, Environmental radiation impact on lifetimes and quasiparticle tunneling rates of fixed-frequency transmon qubits, Appl. Phys. Lett. **120**, 074002 (2022).

[20] A. P. Vepsäläinen, A. H. Karamlou, J. L. Orrell, A. S. Dogra, B. Loer, F. Vasconcelos, D. K. Kim, A. J. Melville, B. M. Niedzielski, J. L. Yoder *et al.*, Impact of ionizing radiation on superconducting qubit coherence, Nature **584**, 551 (2020).

[21] L. Cardani, F. Valenti, N. Casali, G. Catelani, T. Charpentier, M. Clemenza, I. Colantoni, A. Cruciani, G. D'Imperio, L. Gironi *et al.*, Reducing the impact of radioactivity on quantum circuits in a deep-underground facility, Nat. Commun. **12**, 2733 (2021).

[22] F. D. Dominicis, T. Roy, A. Mariani, M. Bal, N. Casali, I. Colantoni, F. Crisa, A. Cruciani, F. Ferroni, D. L. Helis, L. Pagnanini, V. Pettinacci, R. M. Pilipenko, S. Pirro, A. Puiu, A. Romanenko, D. V. Zanten, S. Zhu, A. Grassellino, and L. Cardani, Evaluating radiation impact on transmon qubits in above and underground facilities, arXiv:2405.18355.

[23] J. Krause, C. Dickel, E. Vaal, M. Vielmetter, J. Feng, R. Bounds, G. Catelani, J. M. Fink, and Y. Ando, Magnetic field resilience of three-dimensional transmons with thin-film Al/AlO$_x$/Al Josephson junctions approaching 1 T, Phys. Rev. Appl. **17**, 034032 (2022).

[24] A. Blais, R.-S. Huang, A. Wallraff, S. M. Girvin, and R. J. Schoelkopf, Cavity quantum electrodynamics for superconducting electrical circuits: An architecture for quantum computation, Phys. Rev. A **69**, 062320 (2004).

[25] D. Ristè, C. C. Bultink, M. J. Tiggelman, R. N. Schouten, K. W. Lehnert, and L. DiCarlo, Millisecond charge-parity fluctuations and induced decoherence in a superconducting transmon qubit, Nat. Commun. **4**, 1913 (2013).

[26] F. Hassler, A. R. Akhmerov, and C. W. J. Beenakker, The top-transmon: A hybrid superconducting qubit for parity-protected quantum computation, New J. Phys. **13**, 095004 (2011).

[27] T. Hyart, B. van Heck, I. C. Fulga, M. Burrello, A. R. Akhmerov, and C. W. J. Beenakker, Flux-controlled quantum computation with majorana fermions, Phys. Rev. B **88**, 035121 (2013).

[28] F. Luthi, T. Stavenga, O. W. Enzing, A. Bruno, C. Dickel, N. K. Langford, M. A. Rol, T. S. Jespersen, J. Nygård, P. Krogstrup, and L. DiCarlo, Evolution of nanowire transmon qubits and their coherence in a magnetic field, Phys. Rev. Lett. **120**, 100502 (2018).

[29] J. G. Kroll, W. Uilhoorn, K. L. van der Enden, D. de Jong, K. Watanabe, T. Taniguchi, S. Goswami, M. C. Cassidy, and L. P. Kouwenhoven, Magnetic field compatible circuit quantum electrodynamics with graphene Josephson junctions, Nat. Commun. **9**, 4615 (2018).

[30] A. Kringhøj, T. W. Larsen, O. Erlandsson, W. Uilhoorn, J. G. Kroll, M. Hesselberg, R. P. G. McNeil, P. Krogstrup, L. Casparis, C. M. Marcus, and K. D. Petersson, Magnetic-field-compatible superconducting transmon qubit, Phys. Rev. Appl. **15**, 054001 (2021).

[31] W. Uilhoorn, J. G. Kroll, A. Bargerbos, S. D. Nabi, C.-K. Yang, P. Krogstrup, L. P. Kouwenhoven, A. Kou, and G. de Lange, Quasiparticle trapping by orbital effect in a hybrid superconducting-semiconducting circuit, arXiv:2105.11038.

[32] H. Paik, D. I. Schuster, L. S. Bishop, G. Kirchmair, G. Catelani, A. P. Sears, B. R. Johnson, M. J. Reagor, L. Frunzio, L. I. Glazman, S. M. Girvin, M. H. Devoret, and R. J. Schoelkopf, Observation of high coherence in Josephson junction qubits measured in a three-dimensional circuit QED architecture, Phys. Rev. Lett. **107**, 240501 (2011).

[33] C. Kurter, C. E. Murray, R. T. Gordon, B. B. Wymore, M. Sandberg, R. Shelby, A. Eddins, V. P. Adiga, A. D. K. Finck, E. Rivera *et al.*, Quasiparticle tunneling as a probe of Josephson junction barrier and capacitor material in superconducting qubits, npj Quantum Inf. **8**, 31 (2022).

[34] D. M. Tennant, L. A. Martinez, K. M. Beck, S. R. O'Kelley, C. D. Wilen, R. McDermott, J. L. DuBois, and Y. J. Rosen, Low-frequency correlated charge-noise measurements across multiple energy transitions in a tantalum transmon, PRX Quantum **3**, 030307 (2022).

[35] S. Diamond, V. Fatemi, M. Hays, H. Nho, P. D. Kurilovich, T. Connolly, V. R. Joshi, K. Serniak, L. Frunzio, L. I. Glazman, and M. H. Devoret, Distinguishing parity-switching mechanisms in a superconducting qubit, PRX Quantum **3**, 040304 (2022).

[36] T. Connolly, P. D. Kurilovich, S. Diamond, H. Nho, C. G. L. Bøttcher, L. I. Glazman, V. Fatemi, and M. H. Devoret, Coexistence of nonequilibrium density and equilibrium energy distribution of quasiparticles in a superconducting qubit, Phys. Rev. Lett. **132**, 217001 (2024).

[37] G. Marchegiani, L. Amico, and G. Catelani, Quasiparticles in superconducting qubits with asymmetric junctions, PRX Quantum **3**, 040338 (2022).

[38] K. Serniak, S. Diamond, M. Hays, V. Fatemi, S. Shankar, L. Frunzio, R. J. Schoelkopf, and M. H. Devoret, Direct dispersive monitoring of charge parity in offset-charge-sensitive transmons, Phys. Rev. Appl. **12**, 014052 (2019).

[39] E. Ginossar and E. Grosfeld, Microwave transitions as a signature of coherent parity mixing effects in the Majorana-transmon qubit, Nat. Commun. **5**, 4772 (2014).

[40] P. Joyez, P. Lafarge, A. Filipe, D. Esteve, and M. H. Devoret, Observation of parity-induced suppression of Josephson tunneling in the superconducting single electron transistor, Phys. Rev. Lett. **72**, 2458 (1994).

[41] J. Aumentado, M. W. Keller, J. M. Martinis, and M. H. Devoret, Nonequilibrium quasiparticles and 2*e* periodicity in single-Cooper-pair transistors, Phys. Rev. Lett. **92**, 066802 (2004).

[42] R. M. Lutchyn, L. I. Glazman, and A. I. Larkin, Kinetics of the superconducting charge qubit in the presence of a quasiparticle, Phys. Rev. B **74**, 064515 (2006).

[43] A. A. Houck, J. A. Schreier, B. R. Johnson, J. M. Chow, J. Koch, J. M. Gambetta, D. I. Schuster, L. Frunzio, M. H. Devoret, S. M. Girvin, and R. J. Schoelkopf, Controlling the spontaneous emission of a superconducting transmon qubit, Phys. Rev. Lett. **101**, 080502 (2008).

[44] B. G. Christensen, C. D. Wilen, A. Opremcak, J. Nelson, F. Schlenker, C. H. Zimonick, L. Faoro, L. B. Ioffe, Y. J. Rosen, J. L. DuBois, B. L. T. Plourde, and R. McDermott, Anomalous charge noise in superconducting qubits, Phys. Rev. B **100**, 140503(R) (2019).

[45] P. Fulde, High field superconductivity in thin films, Adv. Phys. **22**, 667 (1973).

[46] R. Meservey and P. Tedrow, Spin-polarized electron tunneling, Phys. Rep. **238**, 173 (1994).

[47] P. Chubov, V. Eremenko, and Y. A. Pilipenko, Dependence of the critical temperature and energy gap on the thickness of superconducting aluminum films, Sov. Phys. JETP **28**, 389 (1969).

[48] R. Meservey and P. M. Tedrow, Properties of very thin aluminum films, J. Appl. Phys. **42**, 51 (1971).

[49] See Supplemental Material at http://link.aps.org/supplemental/10.1103/PhysRevApplied.22.044063, which provides experimental details and additional data and analysis

supporting the claims in the main text and where Refs. [79–82] are cited.

[50] M. Tinkham, *Introduction to Superconductivity* (Dover Publications, Mineola, NY, USA, 2004), 2nd ed.

[51] More generally, given the penetration depths λ_T, λ_B and the film thicknesses of the two electrodes t_T, t_R, the effective thickness determining the characteristic Fraunhofer field amounts to $\lambda_T \tanh(t_T/2\lambda_T) + \lambda_B \tanh(t_B/2\lambda_B) + t_{\mathrm{AlOx}}$, where t_{AlOx} is the thickness of the insulating oxide barrier of the Josephson junction.

[52] D. Willsch *et al.*, Observation of Josephson harmonics in tunnel junctions, Nat. Phys. **20**, 815 (2024).

[53] G. Catelani, Parity switching and decoherence by quasiparticles in single-junction transmons, Phys. Rev. B **89**, 094522 (2014).

[54] M. Houzet, K. Serniak, G. Catelani, M. H. Devoret, and L. I. Glazman, Photon-assisted charge-parity jumps in a superconducting qubit, Phys. Rev. Lett. **123**, 107704 (2019).

[55] J. Braumüller, M. Sandberg, M. R. Vissers, A. Schneider, S. Schlör, L. Grünhaupt, H. Rotzinger, M. Marthaler, A. Lukashenko, A. Dieter, A. V. Ustinov, M. Weides, and D. P. Pappas, Concentric transmon qubit featuring fast tunability and an anisotropic magnetic dipole moment, Appl. Phys. Lett. **108**, 032601 (2016).

[56] S. Majumder, T. Bera, R. Suresh, and V. Singh, A fast tunable 3D-transmon architecture for superconducting qubit-based hybrid devices, J. Low Temp. Phys. **207**, 210 (2022).

[57] P. B. Fischer and G. Catelani, Nonequilibrium quasiparticle distribution in superconducting resonators: Effect of pair-breaking photons, SciPost Phys. **17**, 070 (2024).

[58] The gap suppression with temperature can be safely neglected in this range, temperature being much smaller than the critical temperatures of the two electrodes.

[59] C. Wang, Y. Y. Gao, I. M. Pop, U. Vool, C. Axline, T. Brecht, R. W. Heeres, L. Frunzio, M. H. Devoret, G. Catelani *et al.*, Measurement and control of quasiparticle dynamics in a superconducting qubit, Nat. Commun. **5**, 5836 (2014).

[60] D. J. Van Woerkom, A. Geresdi, and L. P. Kouwenhoven, One minute parity lifetime of a NbTiN Cooper-pair transistor, Nat. Phys. **11**, 547 (2015).

[61] O. Rafferty, S. Patel, C. Liu, S. Abdullah, C. Wilen, D. Harrison, and R. McDermott, Spurious antenna modes of the transmon qubit, arXiv:2103.06803.

[62] C. H. Liu, D. C. Harrison, S. Patel, C. D. Wilen, O. Rafferty, A. Shearrow, A. Ballard, V. Iaia, J. Ku, B. L. T. Plourde, and R. McDermott, Quasiparticle poisoning of superconducting qubits from resonant absorption of pair-breaking photons, Phys. Rev. Lett. **132**, 017001 (2024).

[63] J. H. Nielsen *et al.*, Qcodes/qcodes: Qcodes 0.43.0 (2024).

[64] M. A. Rol, C. Attryde, J. C. van Oven, K. Loh, J. Gloudemans, V. Negîrneac, T. Last, and C. C. Bultink, in *APS March Meeting Abstracts* (2021), Vol. 2021, p. M34–001.

[65] D. Crielaard, D. De Jong, J. Gloudemans, R. Vyas, V. Negirneac, D. Valada, C. Sindile, C. Attryde, A. Lawrence, T. Reynders *et al.*, in *APS March Meeting Abstracts* (2022), Vol. 2022, p. Q36–010.

[66] J. Johansson, P. Nation, and F. Nori, QuTiP 2: A Python framework for the dynamics of open quantum systems, Comput. Phys. Commun. **184**, 1234 (2013).

[67] R. Weiss *et al.*, hmmlearn Python package - hidden Markov models in Python, with scikit-learn like API, https://github.com/hmmlearn/hmmlearn.

[68] https://doi.org/10.5281/zenodo.10728469.

[69] F. Motzoi, J. M. Gambetta, P. Rebentrost, and F. K. Wilhelm, Simple pulses for elimination of leakage in weakly nonlinear qubits, Phys. Rev. Lett. **103**, 110501 (2009).

[70] J. M. Chow, L. DiCarlo, J. M. Gambetta, F. Motzoi, L. Frunzio, S. M. Girvin, and R. J. Schoelkopf, Optimized driving of superconducting artificial atoms for improved single-qubit gates, Phys. Rev. A **82**, 040305(R) (2010).

[71] M. Reed, *Entanglement and quantum error correction with superconducting qubits*, PhD Dissertation, Yale University, 2013.

[72] O. A. E. Cherney and J. Shewchun, Enhancement of superconductivity in thin aluminium films, Can. J. Phys. **47**, 1101 (1969).

[73] A. Barone and G. Paternò, *Physics and Applications of the Josephson Effect* (Wiley, New York, 1982).

[74] L. M. Janssen, G. Butseraen, J. Krause, A. Coissard, L. Planat, N. Roch, G. Catelani, Y. Ando, and C. Dickel, Magnetic-field dependence of a Josephson traveling-wave parametric amplifier and integration into a high-field setup, arXiv:2402.19398.

[75] D. Ristè, S. Poletto, M. Z. Huang, A. Bruno, V. Vesterinen, O. P. Saira, and L. DiCarlo, Detecting bit-flip errors in a logical qubit using stabilizer measurements, Nat. Commun. **6**, 6983 (2015).

[76] U. Vool, I. M. Pop, K. Sliwa, B. Abdo, C. Wang, T. Brecht, Y. Y. Gao, S. Shankar, M. Hatridge, G. Catelani, M. Mirrahimi, L. Frunzio, R. J. Schoelkopf, L. I. Glazman, and M. H. Devoret, Non-Poissonian quantum jumps of a fluxonium qubit due to quasiparticle excitations, Phys. Rev. Lett. **113**, 247001 (2014).

[77] L. Glazman and G. Catelani, Bogoliubov quasiparticles in superconducting qubits, SciPost Phys. Lect. Notes **31**, (2021).

[78] G. Catelani, R. J. Schoelkopf, M. H. Devoret, and L. I. Glazman, Relaxation and frequency shifts induced by quasiparticles in superconducting qubits, Phys. Rev. B **84**, 064517 (2011).

[79] M. J. Peterer, S. J. Bader, X. Jin, F. Yan, A. Kamal, T. J. Gudmundsen, P. J. Leek, T. P. Orlando, W. D. Oliver, and S. Gustavsson, Coherence and decay of higher energy levels of a superconducting transmon qubit, Phys. Rev. Lett. **114**, 010501 (2015).

[80] A. Morvan, V. V. Ramasesh, M. S. Blok, J. M. Kreikebaum, K. O'Brien, L. Chen, B. K. Mitchell, R. K. Naik, D. I. Santiago, and I. Siddiqi, Qutrit randomized benchmarking, Phys. Rev. Lett. **126**, 210504 (2021).

[81] T. F. Mörstedt, W. S. Teixeira, A. Viitanen, H. Kivijärvi, M. Tiiri, M. Rasola, A. M. Gunyho, S. Kundu, L. Lattier, V. Vadimov, G. Catelani, V. Sevriuk, J. Heinsoo, J. Räbinä, J. Ankerhold, and M. Möttönen, Rapid on-demand generation of thermal states in superconducting quantum circuits, arXiv:2402.09594.

[82] A. Sultanov, M. Kuzmanović, A. V. Lebedev, and G. S. Paraoanu, Protocol for temperature sensing using a three-level transmon circuit, Appl. Phys. Lett. **119**, 144002 (2021).